Supporting Information

Engineering Efficient Bifunctional Electrocatalysts for Rechargeable Zinc–Air Batteries by Con-fining Fe-Co-Ni Nanoalloys in Nitrogen-Doped Carbon Nanotube@Nanosheet Frameworks

Xiannong Tang,[†,a] Rui Cao,[†,b] Longbin Li,[a] Bingyu Huang,[a] Weijuan Zhai,[a] Kai Yuan,[*,a] and Yi-wang Chen[*,a,c]

[a] Institute of Polymers and Energy Chemistry (IPEC), College of Chemistry, Nanchang University, Nanchang 330031, China

[b] Stanford Synchrotron Radiation Lightsource (SSRL), SLAC National Accelerator Laboratory, Menlo Park, CA 94025, United States

[c] Institute of Advanced Scientific Research (iASR), Jiangxi Normal University, Nanchang 330022, China

[†] These authors contributed equally to this work.

* Corresponding authors. E-mails: kai.yuan@ncu.edu.cn; ywchen@ncu.edu.cn

Table of Contents:

X-ray Adsorption Spectra

A Si(220) double crystal monochromator was used for energy selection. The monochromator was detuned by 30 to 40% to diminish components from higher harmonics. The solid samples were pressed into palettes using cellulose as binder and diluent. The samples were installed on a cryogenic sample rod and kept inside a liquid helium CryoIndustries cryocooler at ~10 K during data collection. The first inflection point of the metal foil spectrum was used for energy calibration. EXAFS data was measured to k = 13 $Å^{-1}$ (fluorescence mode) using a Lytle or Canberra Germanium 30-element array detector. Internal energy calibration was accomplished by simultaneous measurement of the absorption of a Metal-foil placed between two ionization chambers situated after the sample probe. XAS data from the Germanium detector were processed using SamView of the Sixpack software and the averaged spectrum was saved and imported to the Athena program. The pre-edge region was normalized by fitting a second order polynomial and subtracting this from the entire spectrum as background. A four-region spline of orders 2, 3, 3 and 3 was used to model the smoothly decaying post-edge region. The data were normalized by subtracting the cubic spline and assigning the edge jump to 1.0 using the Athena program. The XAFS and FT-XAFS were fitted using the Artemis software. The structural parameters varied during the fitting process were the bond distance (*R*) and the bond variance σ^2, which is related to the Debye-Waller factor resulting from thermal motion, and static disorder of the absorbing and scattering atoms. Coordination numbers were also varied during the fit.

DFT Computational Details

All DFT computations with spin-polarized were carried out using Vienna ab initio simulation package (VASP).[1,2] The projector augmented wave method and general gradient approximation in the Perdew–Burke–Ernzerhof (PBE) form was applied to describe the interactions of ion-electron.[3–5] The D3 method by Grimme was applied to approximately account for the dispersion interactions.[6] During the structure relaxation, the setup of convergence criterion for residual force and energy was 0.03 eV/Å and 10^{-5} eV, respectively. Brillouin zones were sampled by a Monkhorst–Pack k–point mesh with a 3 × 3 × 1 k–point grid. A vacuum space of 20 Å was employed to avoid the interaction between two periodic units.

The free energy change (ΔG) of each ORR/OER elementary reaction was calculated as

$$\Delta G = \Delta E + \Delta E_{ZPE} - T\Delta S$$

where ΔE, E_{ZPE}, T and S are the reaction energy difference, zero–point energies, temperature and entropy, respectively.

The theoretical overpotential η was determined by the potential limiting step:

$$\eta = \max [\Delta G_1, \Delta G_2, \Delta G_3, \Delta G_4]/e - U_{equilibrium}\ (V)$$

where $U_{equilibrium}$ is the equilibrium potential (1.23 V and –1.23 V for OER and ORR, respectively).

Electrochemical Measurements

All data were recorded on an AutoLab PGSTAT302Nl with PINE AFMSRCE. The three-electrode system was installed as follow: the working electrode (WE) was a RDE (disk area: 0.196 cm^2) or a RRDE (disk area: 0.1866 cm^2, ring area: 0.2475 cm^2); the reference electrode (RE) was an Ag/AgCl

electrode; a graphite rod was employed for the counter electrode (CE). The electrolyte was 0.1 M KOH aqueous solution and purge of O_2 for 30 min before running tests. The WE was processed as follow: 10 μL of homogenous FeCoNi-NC dispersion (consist of 10.0 mg FeCoNi-NC, 950 μL 50% aqueous ethanol and 50 μL Nafion D520 5% dispersion) was carefully dropcast onto the glassy carbon disk and dried in N_2 flow. Therefore, 0.5 mg cm^{-2} FeCoNi-NC was loaded on the WE.

The ECSA was derived from C_{dl}, which was measured by a series of cyclic voltammetry (CV) scanning in a non-Faradaic potential (1.00-1.10 V) at various scan rates of 1-10 mV s^{-1}.The ECSA was determined by the following equation:[7]

$$ECSA = C_{dl} / C_s$$

where C_s represents the specific capacitance of total double layer (0.04 mF cm^{-2}).

ORR and OER linear sweep voltammetry (LSV) cuves were recorded at a scan rate of 10 mV s^{-1}. The geometric area of electrode was employed to normalize the currents to current densities. The limited current density was set as the value of current density at 0.40 V (vs. RHE). The j_k was determined by Koutecky-Levich (K-L) equation:[8]

$$\frac{1}{j} = \frac{1}{j_L} + \frac{1}{j_k} = \frac{1}{B\omega^{1/2}} + \frac{1}{j_k}$$

where j is current density measured from LSV curves, j_L is the diffusion-limited current density, j_k is the kinetic current density, □ is the angular velocity. B is a constant.

The transferred electrons number (n) was determined by RRDE measurements. According to the results of RRDE experiments, the HO_2^- (%) and the n values can be obtained by the following equations:

$$n = \frac{4 \times I_{Disk}}{I_{Disk} + I_{Ring}/N}$$

$$\%(HO_2^-) = \frac{200 \times I_{Ring}}{I_{Disk} + I_{Ring}/N}$$

where I_{Disk} is the disk current, I_{Ring} is the ring current and the N is 0.37.

Supplementary Figures and Tables

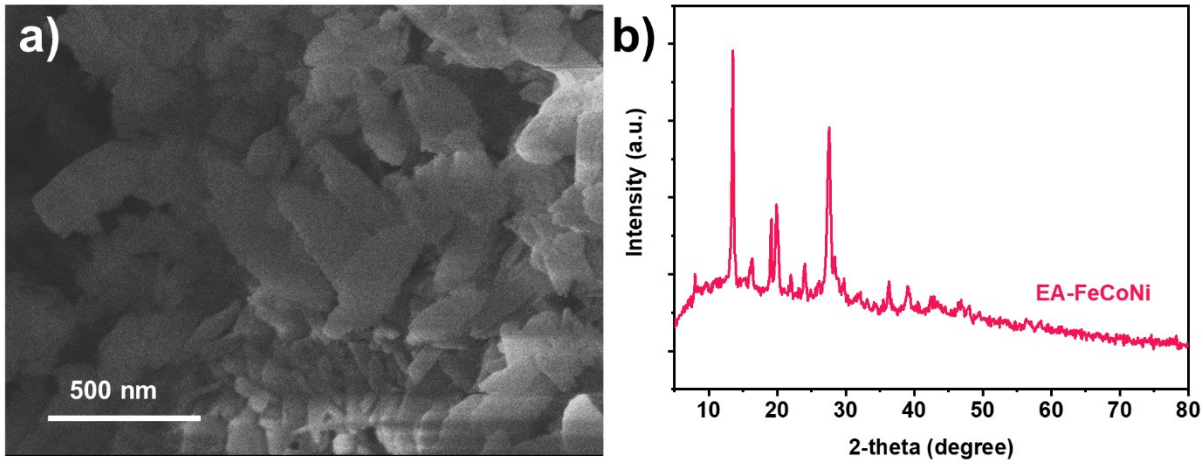

Figure S1. (a) SEM image and (b) XRD pattern of EA-FeCoNi.

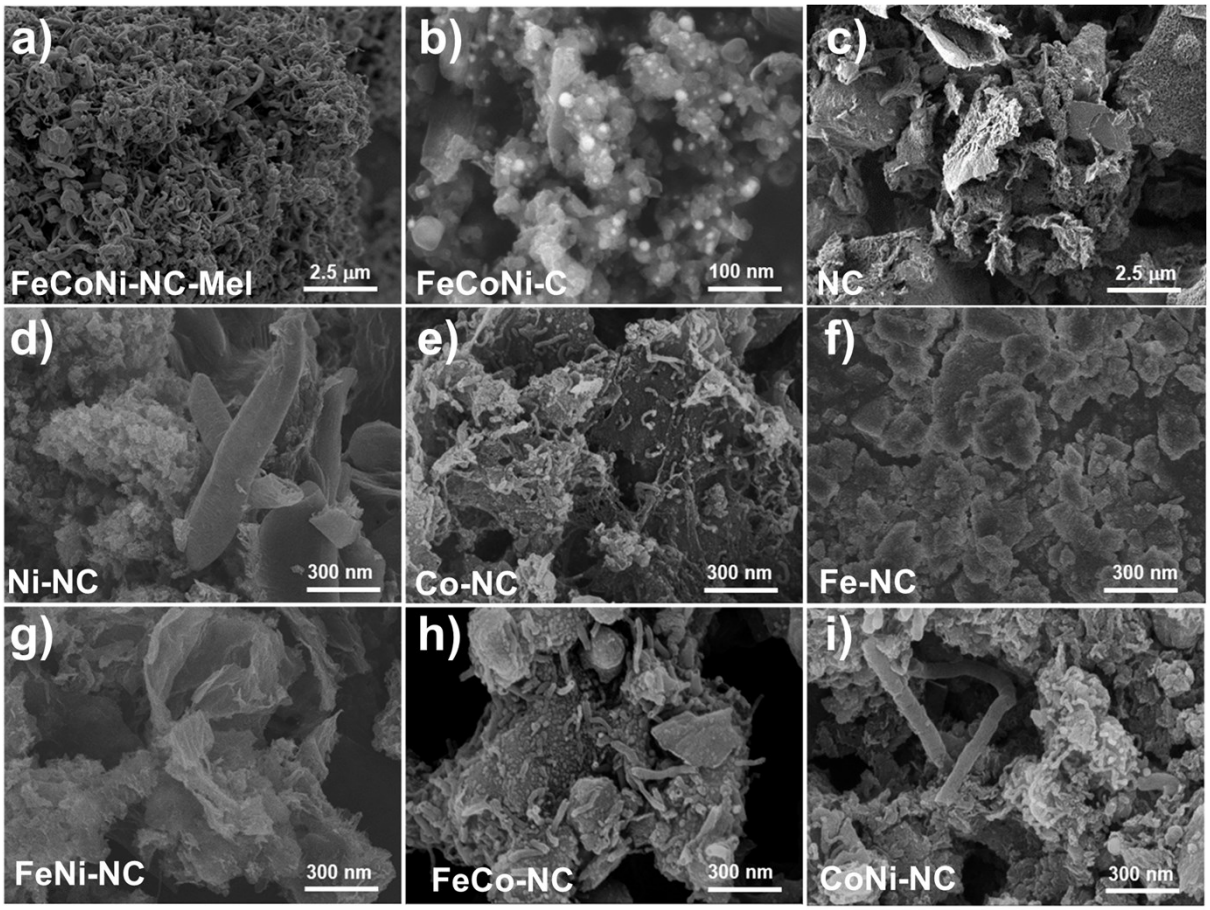

Figure S2. SEM images of (a) FeCoNi-NC-Mel, (b) FeCoNi-C, (c) NC, (d) Ni-NC, (e) Co-NC, (f) Fe-NC, (g) FeNi-NC, (h) FeCo-NC and (i) CoNi-NC.

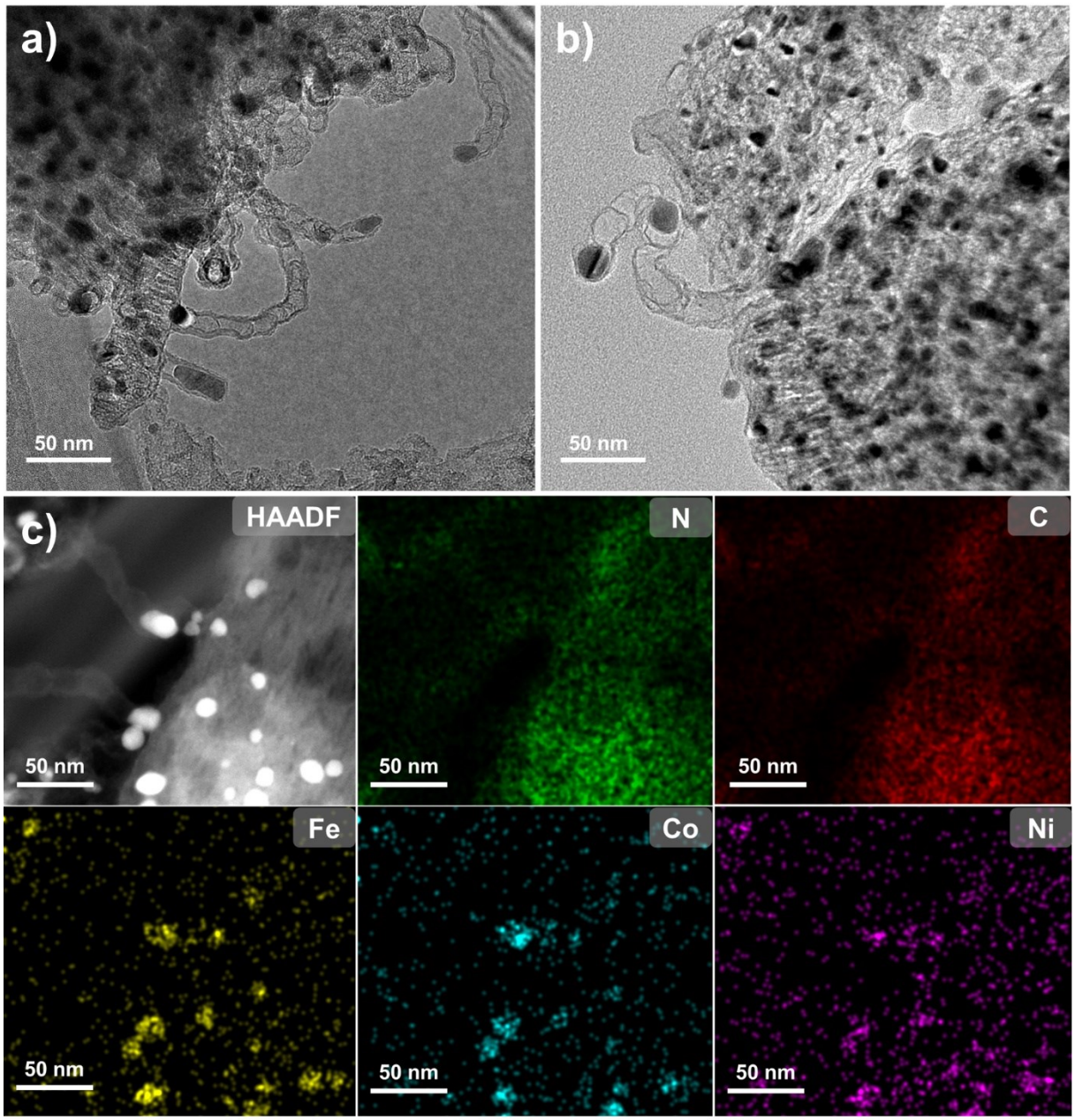

Figure S3. (a) TEM images, (b) HAADF-STEM image and (c) corresponding energy-dispersive X-ray spectroscopy (EDS) mapping of FeCoNi-NC.

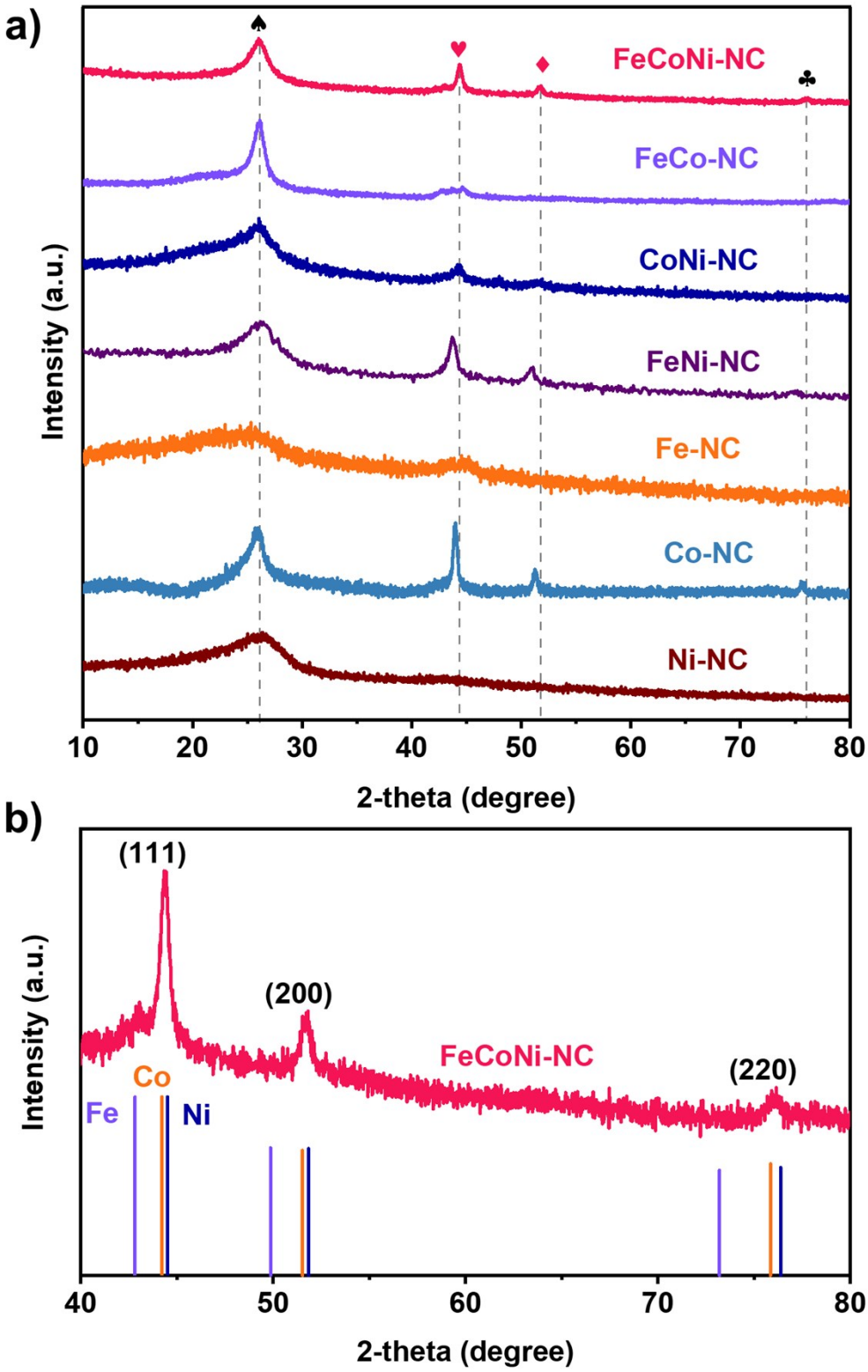

Figure S4. (a) Powder XRD patterns of samples with various metal elements. The spade corresponds to (002) planes of graphitic carbon. The heart, diamond and club correspond to (111), (200) and (022) facets of Fe-Co-Ni alloy, respectively. (b) XRD pattern of FeCoNi-NC.

Table S1. Summary of the Brunauer–Emmett-Teller (BET) surface area and pore size distribution.

Sample	BET surface area (m^2 g^{-1})	micropore volume (cm^3 g^{-1})	micropore width (nm)	mesopore volume (cm^3 g^{-1})	mesopore width (nm)	macropore volume (cm^3 g^{-1})
FeCoNi-NC	398.49	0.055	0.52	0.382	4.08	0.084
FeCo-NC	288.58	0.026	0.48	0.406	4.08	0.144
FeNi-NC	94.49	0.009	2.00	0.173	3.38	0.095
CoNi-NC	269.42	0.033	0.93	0.345	4.22	0.123
Fe-NC	96.60	0.006	1.54	0.138	3.93	0.080
Co-NC	261.02	0.034	0.93	0.392	4.37	0.226
Ni-NC	52.11	N/A	N/A	0.098	3.94	0.049

*Micropore and mesopore were determined using quenched solid density functional theory (QSDFT) method, while the macropore was determined using Barrett-Joyner-Halenda (BJH) method.

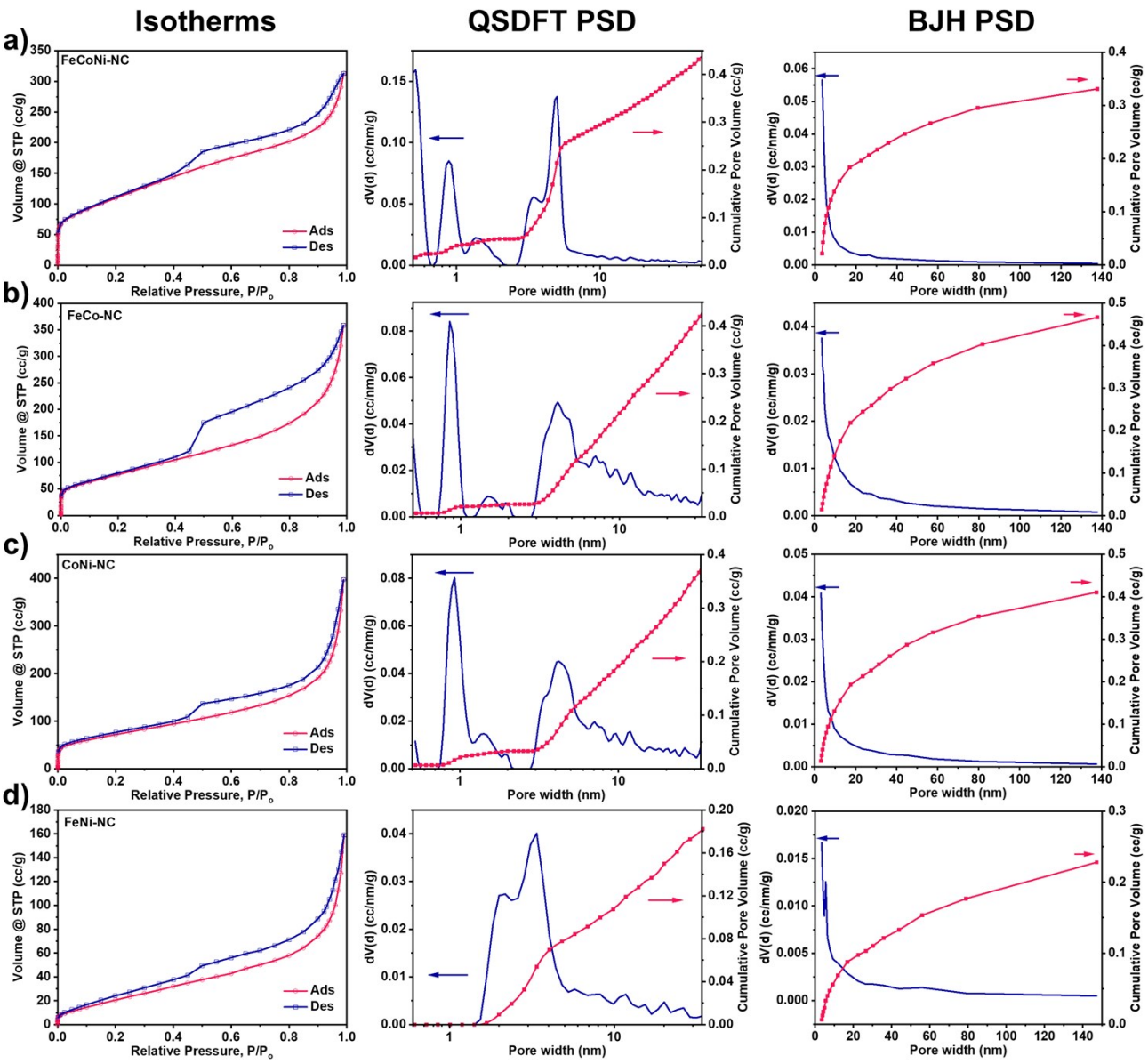

Figure S5. Nitrogen adsorption and desorption isotherms measured at 77 K and corresponding pore size distribution for (a) FeCoNi-NC, (b) FeCo-NC, (c) CoNi-NC, and (d) FeNi-NC.

Table S2. Comparison of BET surface area between FeCoNi-NC and state-of-the-art trimetallic transition metal-based catalysts reported in recent literatures.

Sample	BET surface area (m^2 g^{-1})	References
FeCoNi-NC	**398**	**This work**
N-nGT(FeCoNi)	145	9
FeCo/FeCoNi@NCNTs-HF	212	10
CoNiFe-S MNs	166	11
Fe_2Ni_2N/Co@NCNT	174	12
$Mn_{0.5}(Fe_{0.3}Ni_{0.7})_{0.5}$/MWCNTs-$O_x$	263	13

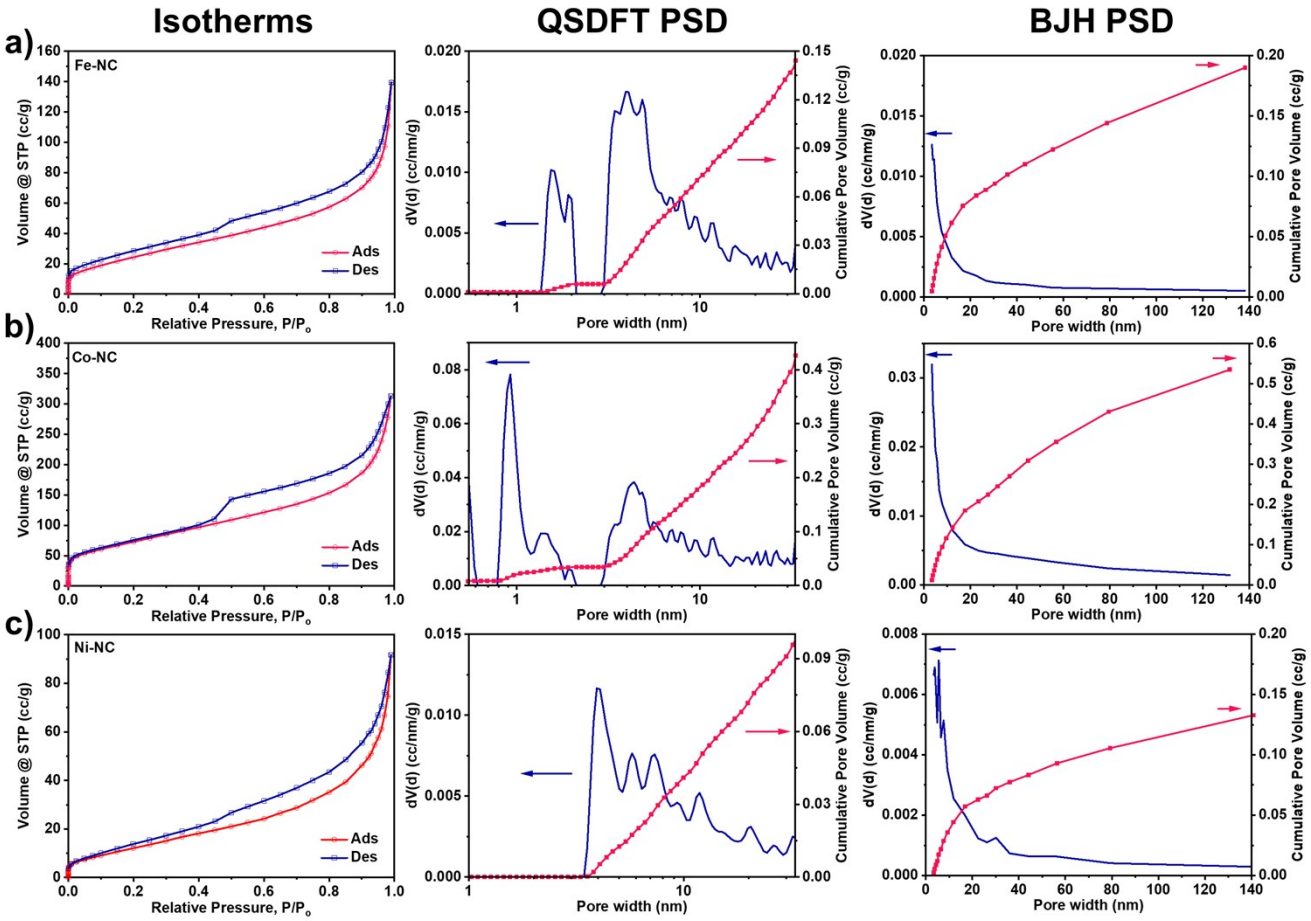

Figure S6. Nitrogen adsorption and desorption isotherms measured at 77 K and corresponding pore size distribution for (a) Fe-NC, (b) Co-NC, and (c) Ni-NC.

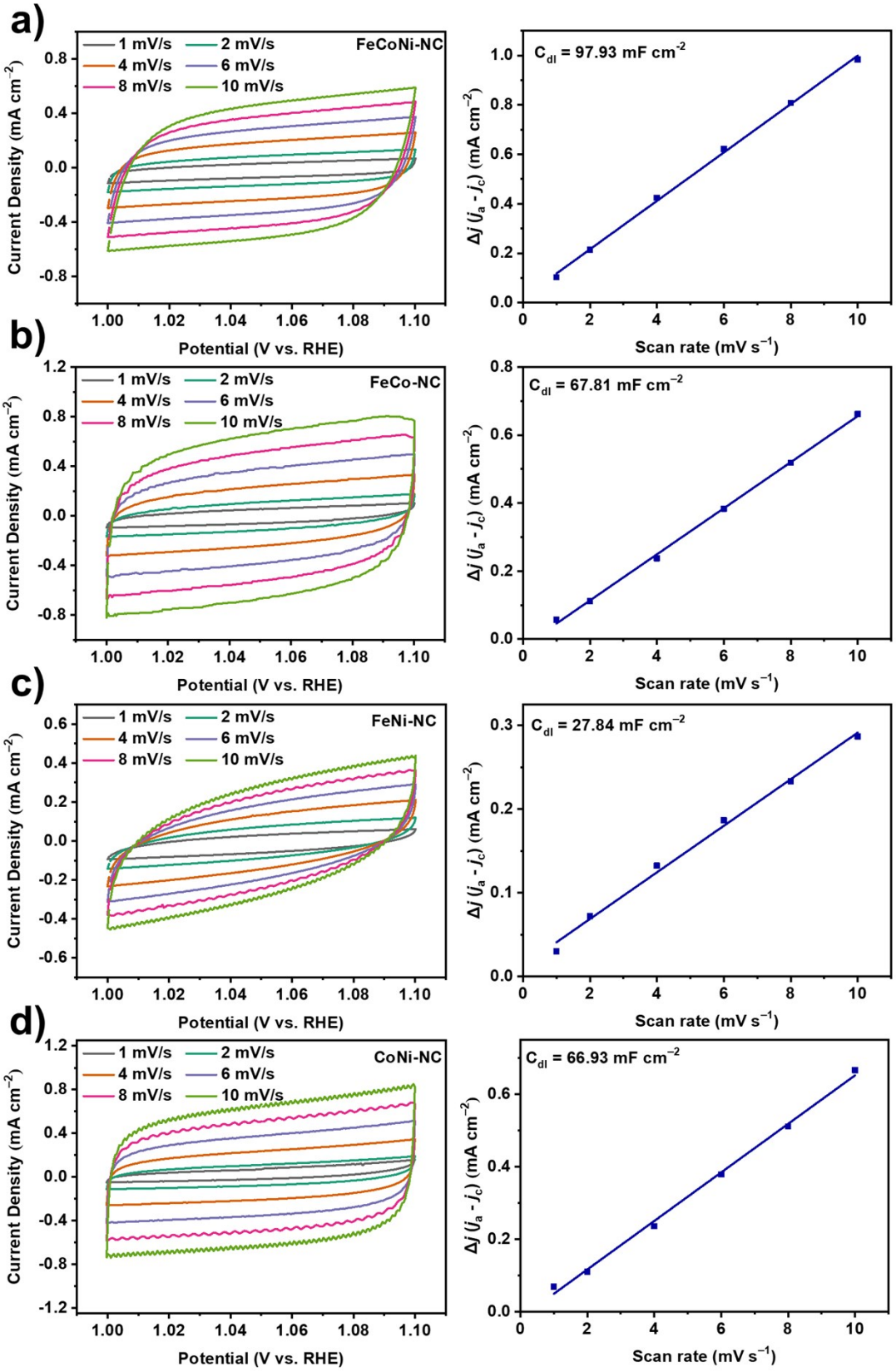

Figure S7. CV curves at different scan rates and corresponding capacitive Δj (j_a-j_c) at the potential of 1.05 V (vs. RHE) plots to estimate the electrochemical double-layer capacitances (C_{dl}) for (a) FeCoNi-NC, (b) FeCo-NC, (c) FeNi-NC and (d) CoNi-NC.

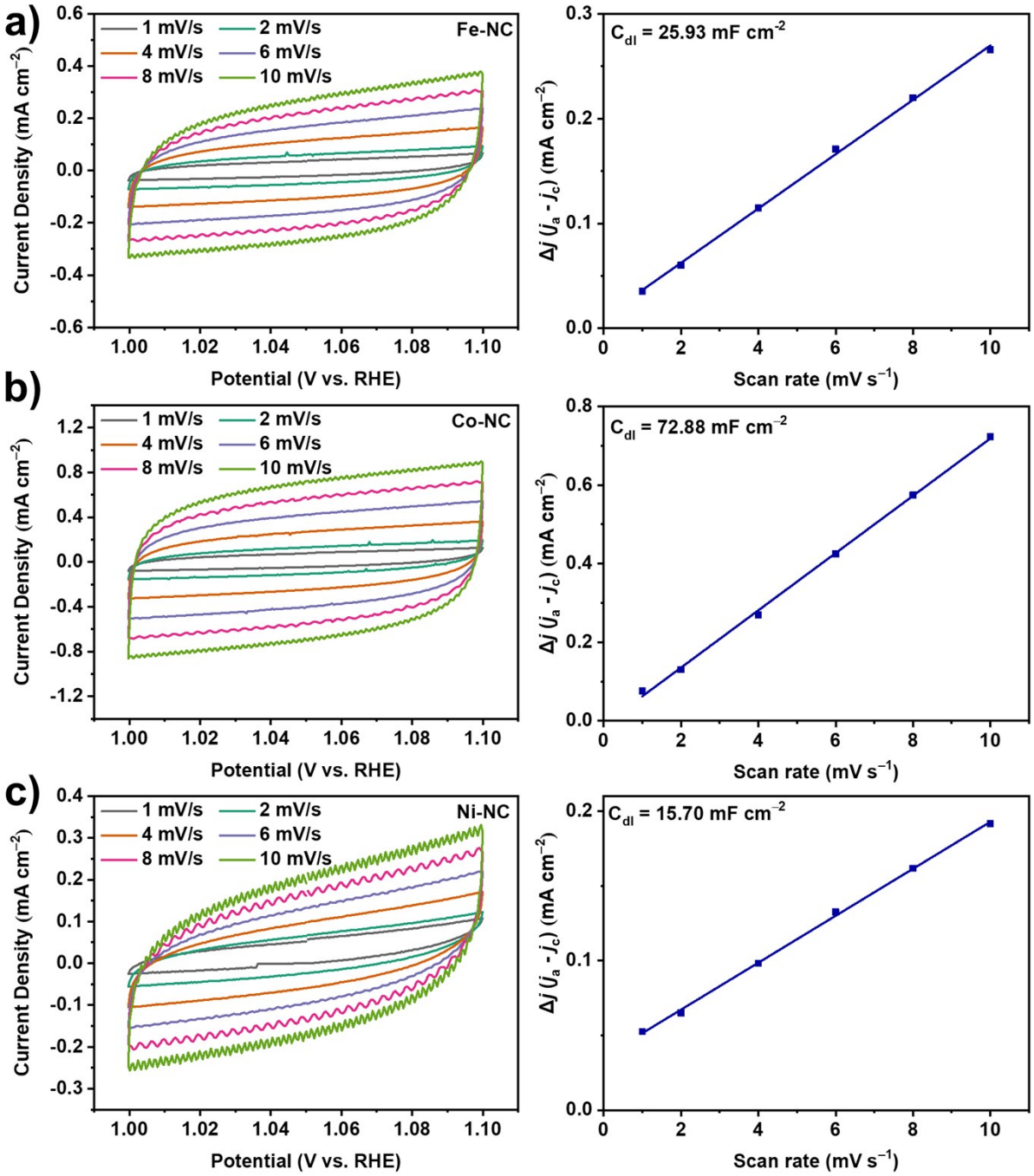

Figure S8. CV curves at different scan rates and corresponding capacitive Δj (j_a-j_c) at the potential of 1.05 V (vs. RHE) plots to estimate the electrochemical double-layer capacitances (C_{dl}) for (a) Fe-NC, (b) Co-NC and (c) Ni-NC.

Table S3. Summary of the effective chemical surface area (ECSA).

Sample	C_{dl} (mF cm^{-2})	ECSA (m^2 g^{-1})
FeCoNi-NC	97.93	244.83
FeCo-NC	67.81	169.53
FeNi-NC	27.84	69.60
CoNi-NC	66.93	167.33
Fe-NC	25.93	64.83
Co-NC	72.88	182.20
Ni-NC	15.70	39.25

Table S4. Inductively coupled plasma optical emission spectrometry (ICP-OES) analysis of FeCoNi-NC.

	Fe	Co	Ni
Element content (mg kg^{-1})	17732	14301	12296
Element content (wt %)	1.77	1.43	1.23
Molar ratio	33.42	39.23	27.35

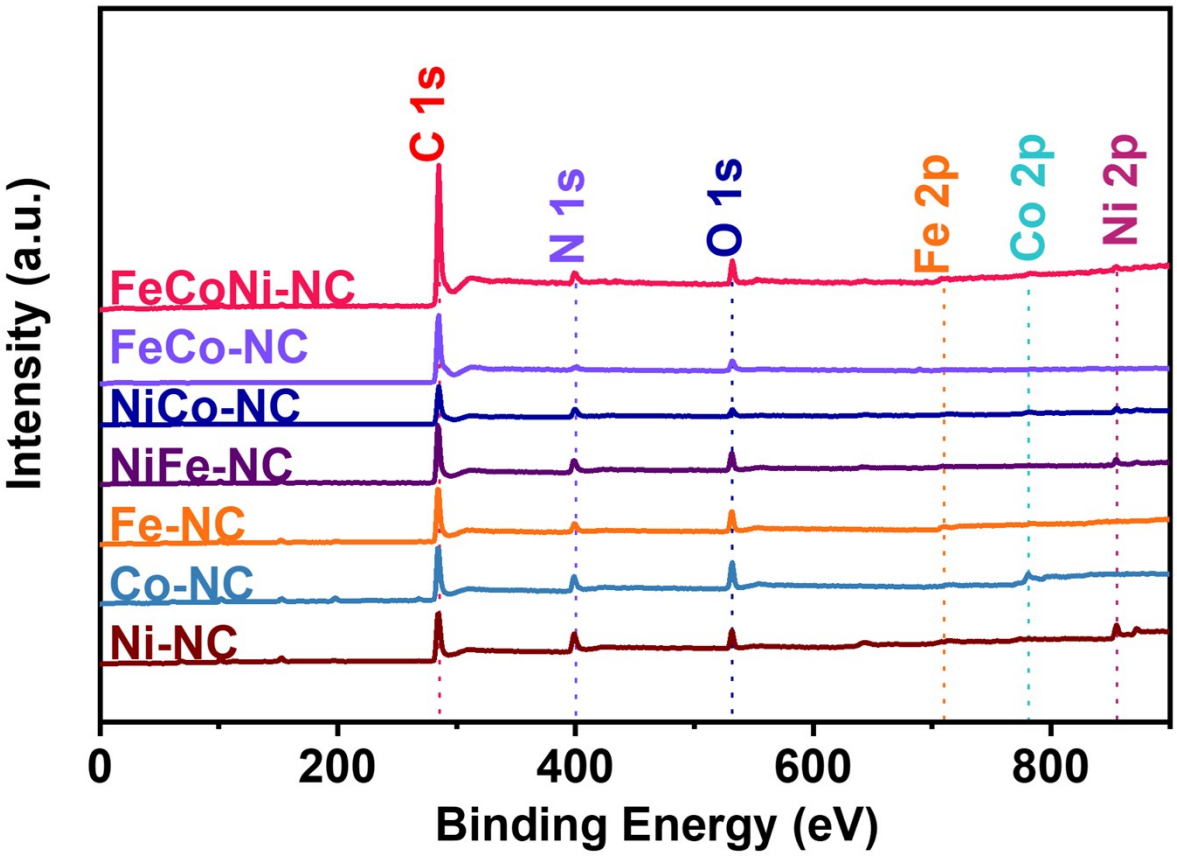

Figure S9. XPS survey spectra of different samples.

Table S5. Elemental contents of C, N, O, Fe, Co and Ni based on XPS analysis for trimetallic, bimetallic and monometallic simples.

Sample	Chemical composition (at %)					
	C	N	O	Fe	Co	Ni
FeCoNi-NC	78.85	10.68	8.53	0.83	0.42	0.69
FeCo-NC	88.31	3.92	7.07	0.26	0.44	--
FeNi-NC	77.80	11.74	9.05	0.55	--	0.86
CoNi-NC	77.51	14.30	6.30	--	0.69	1.20
Fe-NC	78.71	8.84	11.61	0.84	--	--
Co-NC	79.94	13.18	6.10	--	0.78	--
Ni-NC	70.94	17.45	9.47	--	--	2.14

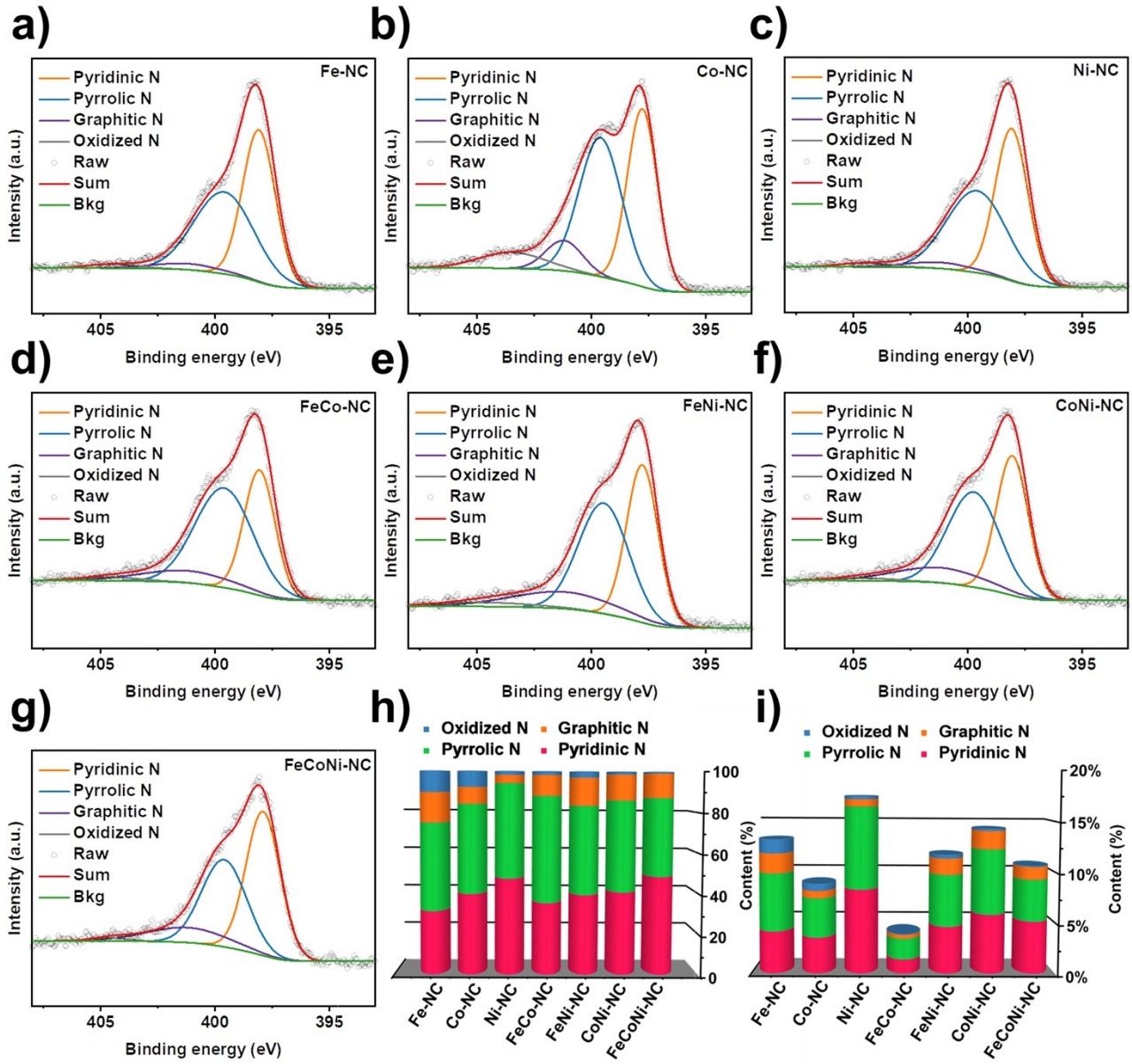

Figure S10. (a-g) High-resolution N 1s XPS spectra for different samples, (h) and (i) relative ratios of the deconvoluted peak areas of the N 1s XPS spectra.

Table S6. Configuation of nitrogen based on N1s high-resolution XPS analysis for trimetallic, bimetallic and monometallic simples.

Simple	Configuation of nitrogen (%)			
	Pyridinic N	Pyrrolic N	Graphitic N	Oxidized N
FeCoNi-NC	48.47	38.65	11.92	0.95
FeCo-NC	35.40	52.55	10.18	1.87
FeNi-NC	39.42	43.74	13.74	3.10
CoNi-NC	40.77	45.05	12.67	1.51
Fe-NC	31.30	43.38	14.88	10.44
Co-NC	39.84	44.04	8.29	7.84
Ni-NC	47.44	46.63	4.02	1.92

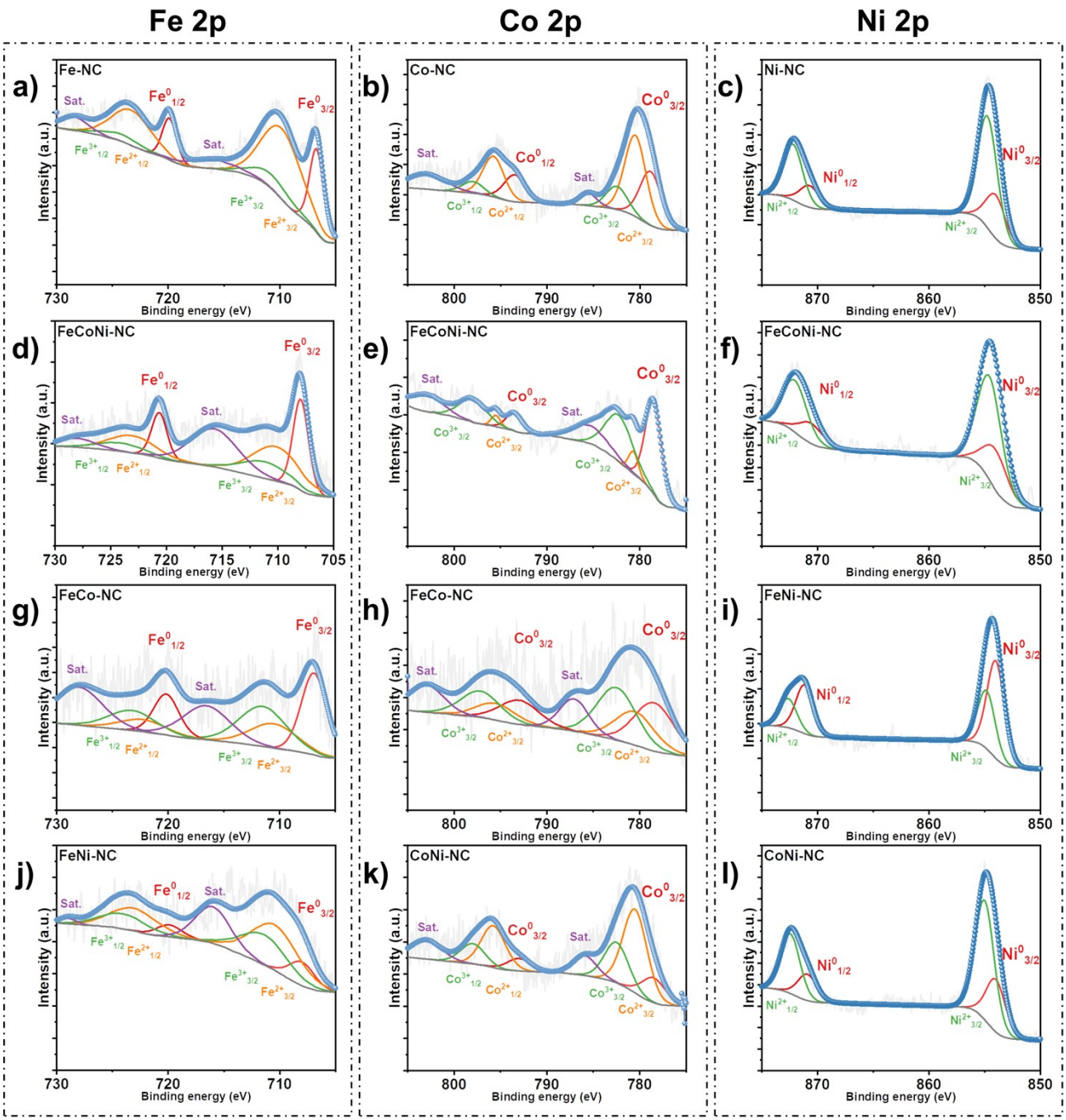

Figure S11. High-resolution (a-d) Fe 2p, (e-h) Co 2p and (i-l) Ni 2p XPS spectra for different samples.

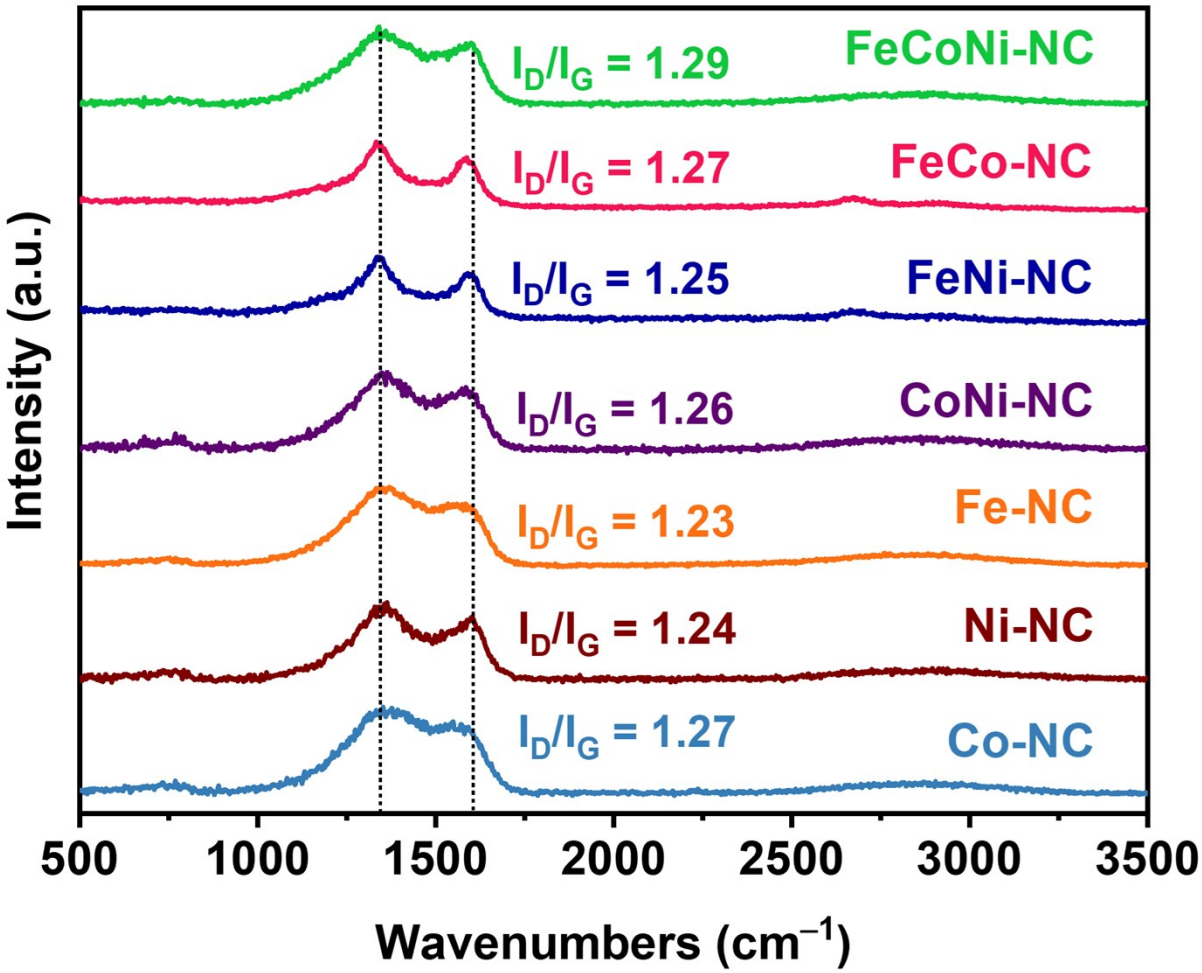

Figure S12. Raman spectra of different samples.

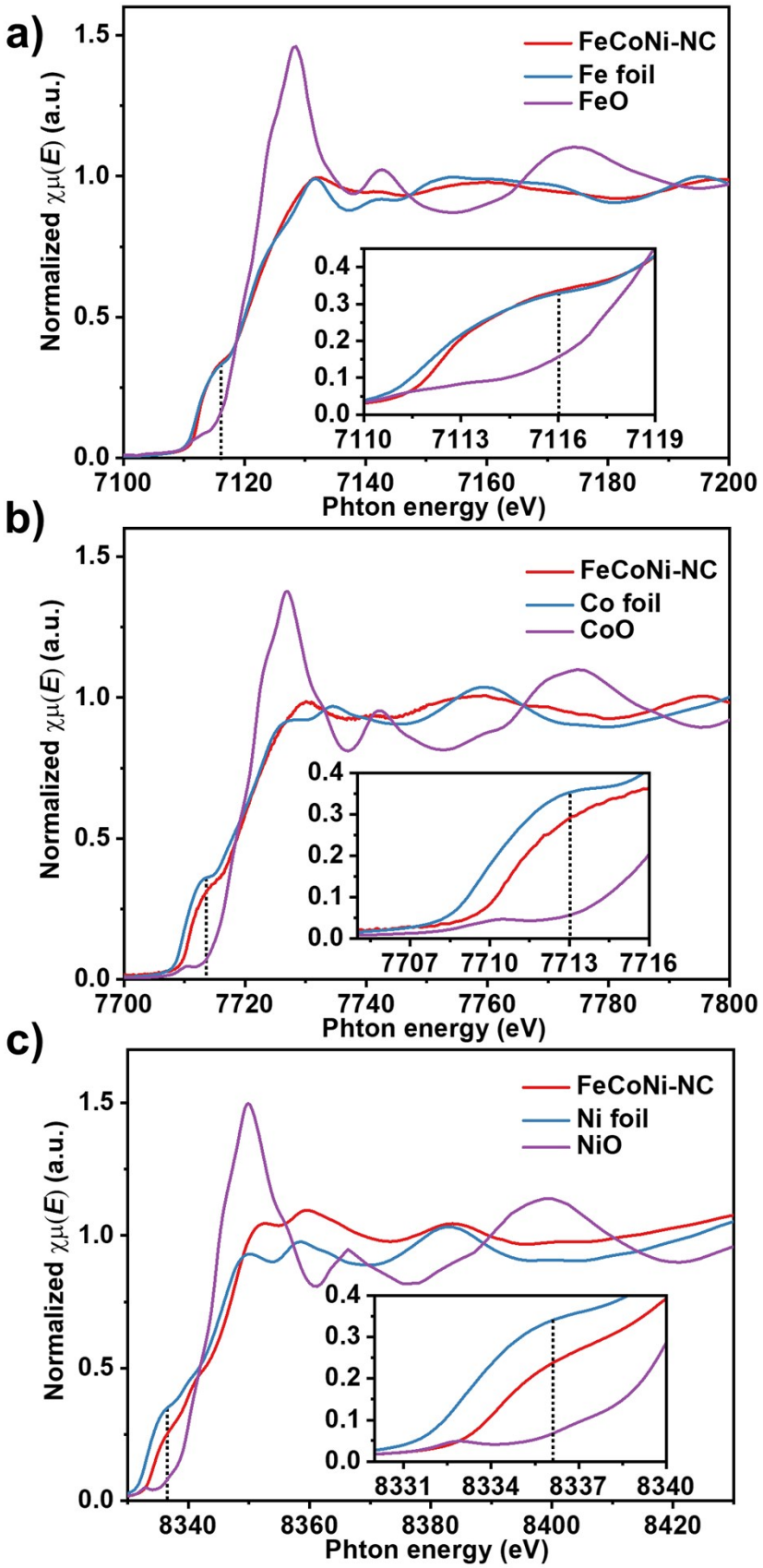

Figure S13. Comparison of (a) Fe K-edge, (b) Co K-edge and (c) Ni K-edge near-edge XANES curves for FeCoNi-NC, reference metal foils and metal oxides.

Table S7. K–edge EXAFS curve fitting parameters for FeCoNi-NC.

Sample	Bond type	CN	Bond length *R* (Å)	Bond disorder s^2 ($Å^2$)	R factor
FeCoNi-NC Co-	Co-Co	9.82 ± 1.73	2.51	0.004	0.01
	Co-Ni/Fe	5.88 ± 1.64	2.71	0.005	0.01
FeCoNi-NC Ni-	Ni-Ni	4.13 ± 0.36	2.48	0.004	0.01
	Ni-Co/Fe	2.63 ± 0.89	3.09	0.005	0.01
FeCoNi-NC Fe-	Fe-Fe	4.79 ± 1.42	2.48	0.002	0.002
	Fe-Ni/Co	2.58 ± 1.75	2.83	0.002	0.01

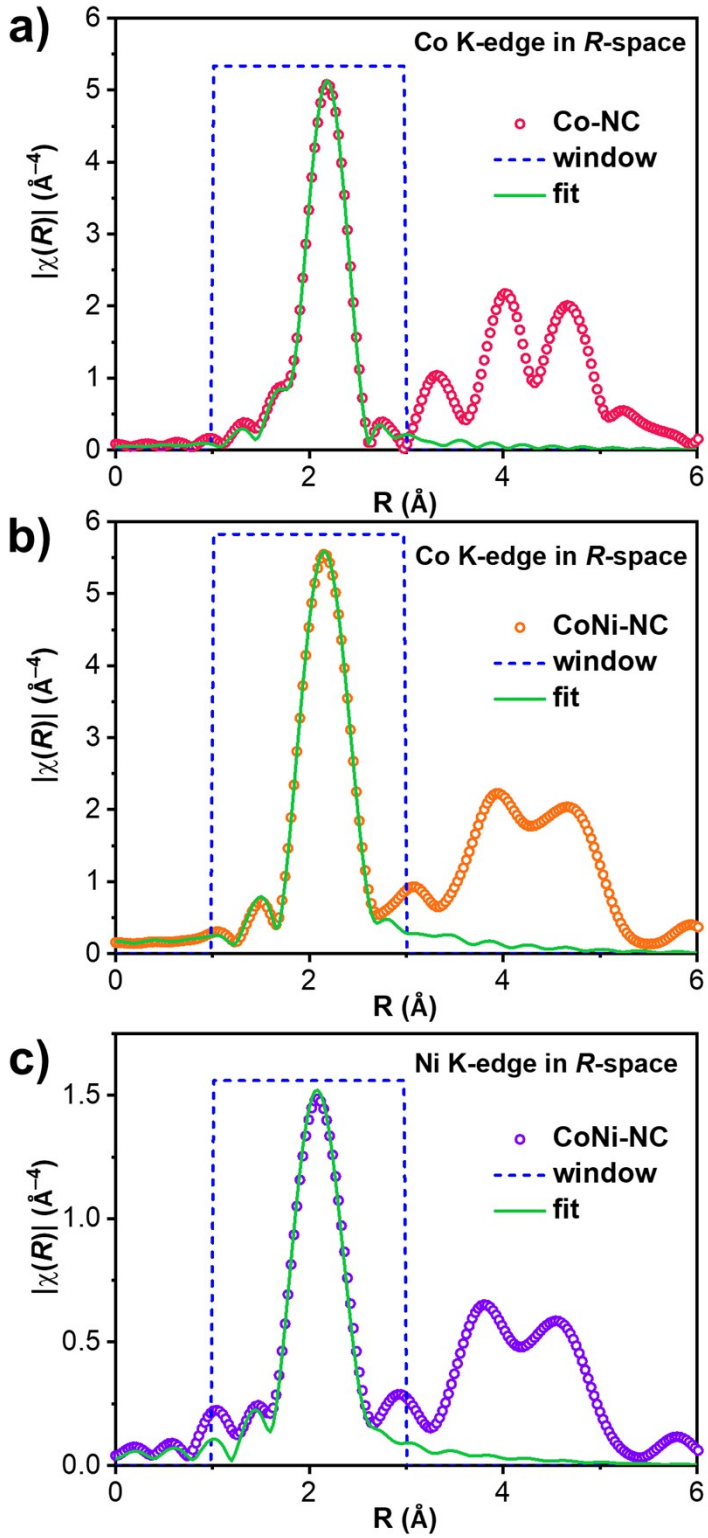

Figure S14. EXAFS analysis in R space for (a) Co K-edge of Co-NC, (b) Co K-edge of CoNi-NC and (c) Ni K-edge of CoNi-NC. The EXAFS fitting is mainly attention to the first shell, and intensity signals in *R* space between 3.3 Å to 5 Å are mainly motivated by multiple scattering, which is unrelated to the metallic bonding and alloy bonding.

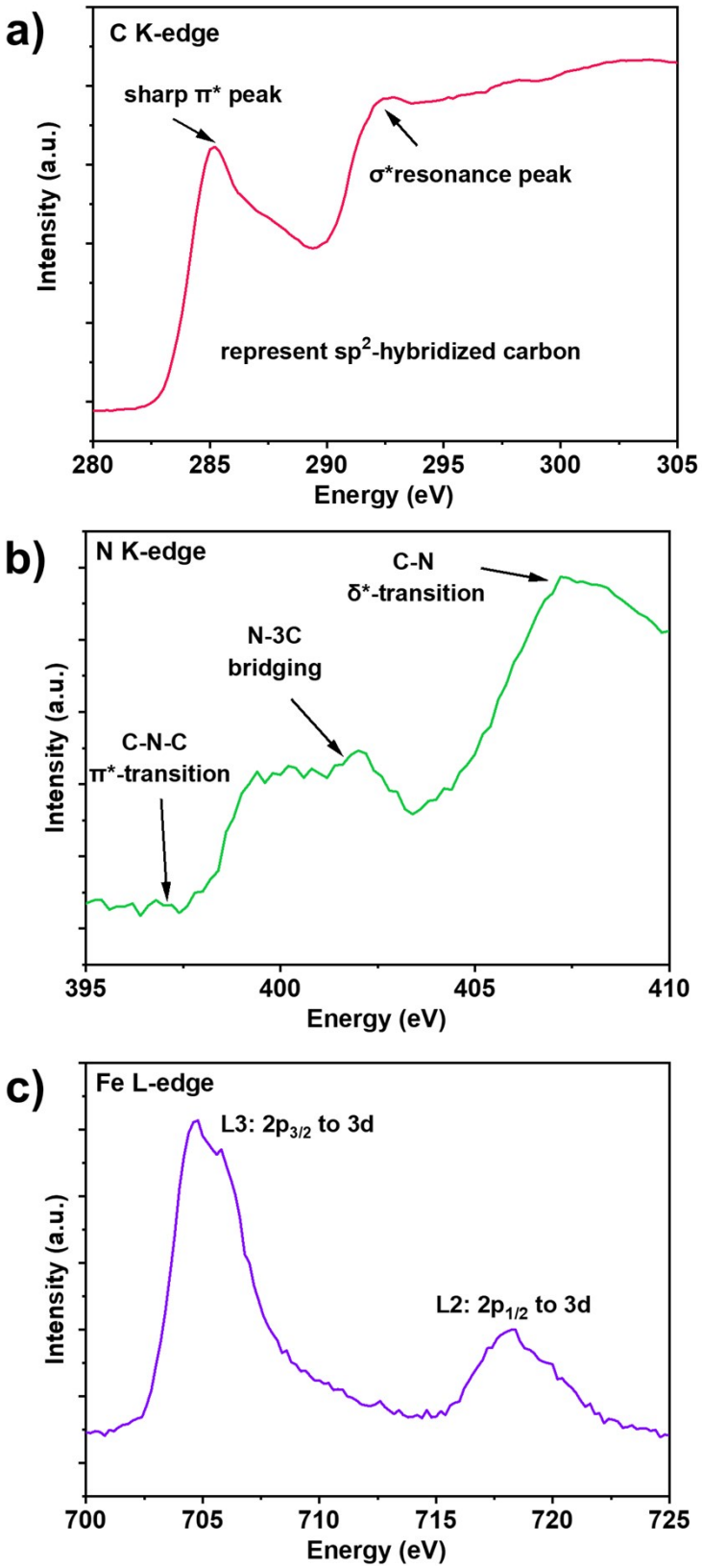

Figure S15. (a) C K-edge (b) N K-edge and (c) Fe L-edge XANES spectra of FeCoNi-NC.

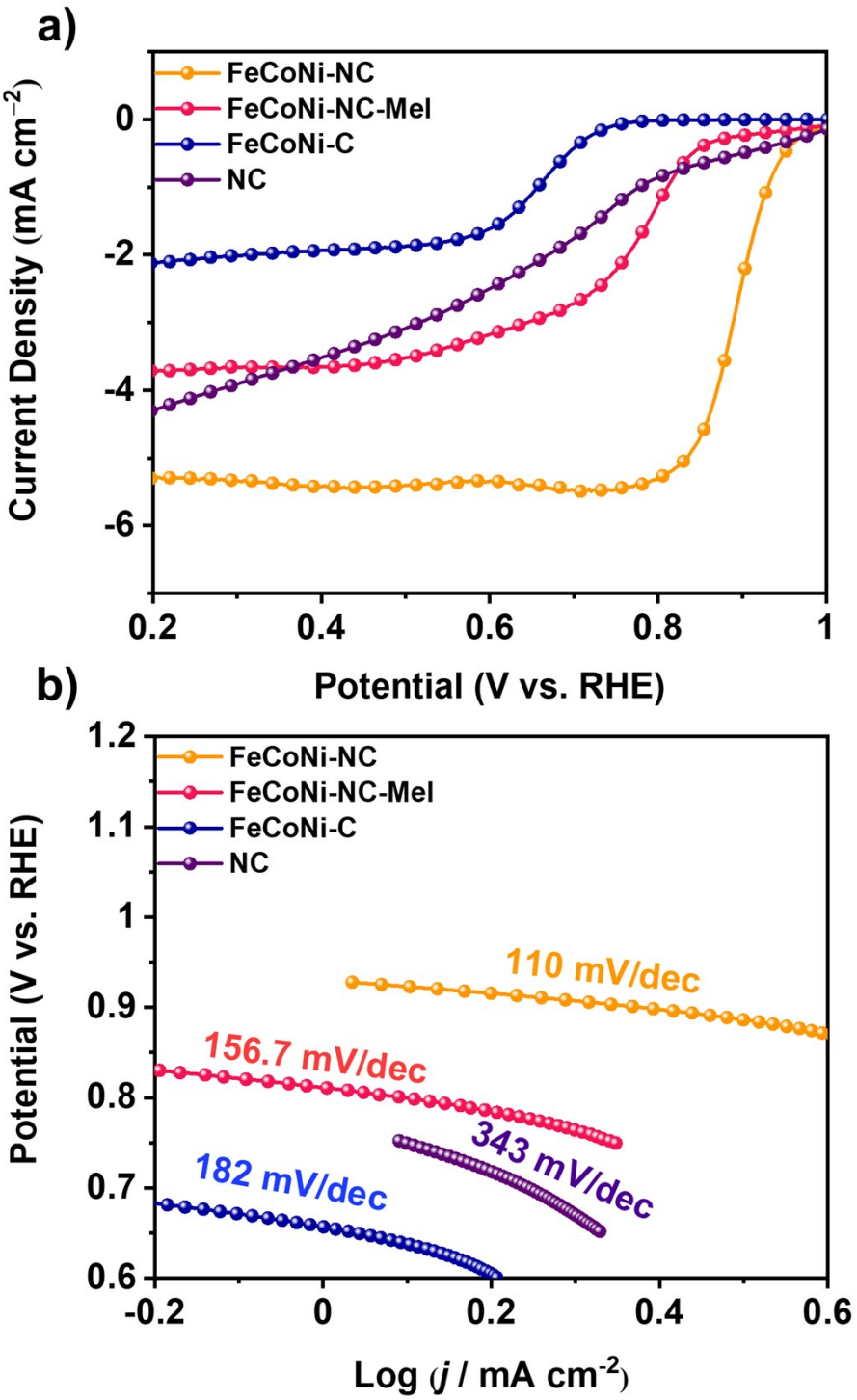

Figure S16. (a) ORR linear sweep voltammetry (LSV) polarization curves and (b) ORR Tafel plots for FeCoNi-NC, FeCoNi-NC-Mel, FeCoNi-C and NC.

Table S8. Comparison of ORR performance of FeCoNi-NC with previously reported advanced alloy-based catalysts in alkaline solution.

Sample	Electrolyte	$E_{1/2}$ (V vs. RHE)	References
N-GCNT/FeCo-3	0.1M KOH	0.92	14
C@NCF-900	0.1M KOH	0.93	15
CoNiFe-S MNs	0.1M KOH	0.78	11
CoFe/N-GCT	0.1M KOH	0.79	16
FeCo-N_x-CN	0.1M KOH	0.89	17
CoNi@NCNT/NF	0.1M KOH	0.87	18
FeCo-DHO/NCNTs	1 M KOH	0.86	19
Fe_2Ni_2N/Co@NCNT	0.1M KOH	0.76	12
FeCo/FeCoNi@NCNTs-HF	0.1M KOH	0.85	20
CoFe-PPy	0.1 M KOH	0.84	21
$Mn_{0.5}(Fe_{0.3}Ni_{0.7})_{0.5}O_x$	0.1M KOH	0.84	13
NiFe/N-CNT	0.1M KOH	0.75	21
G-$Co_{0.6}Fe_{0.4}$	0.1 M KOH	0.83	22
FeCo/Co_2P@NPCF	0.1 M KOH	0.79	23
Co_2Fe_1@NC	0.1 M KOH	0.85	24
Pt/C-RuO_2	**0.1 M KOH**	**0.85**	**This work**
FeCoNi-NC	**0.1 M KOH**	**0.89**	**This work**

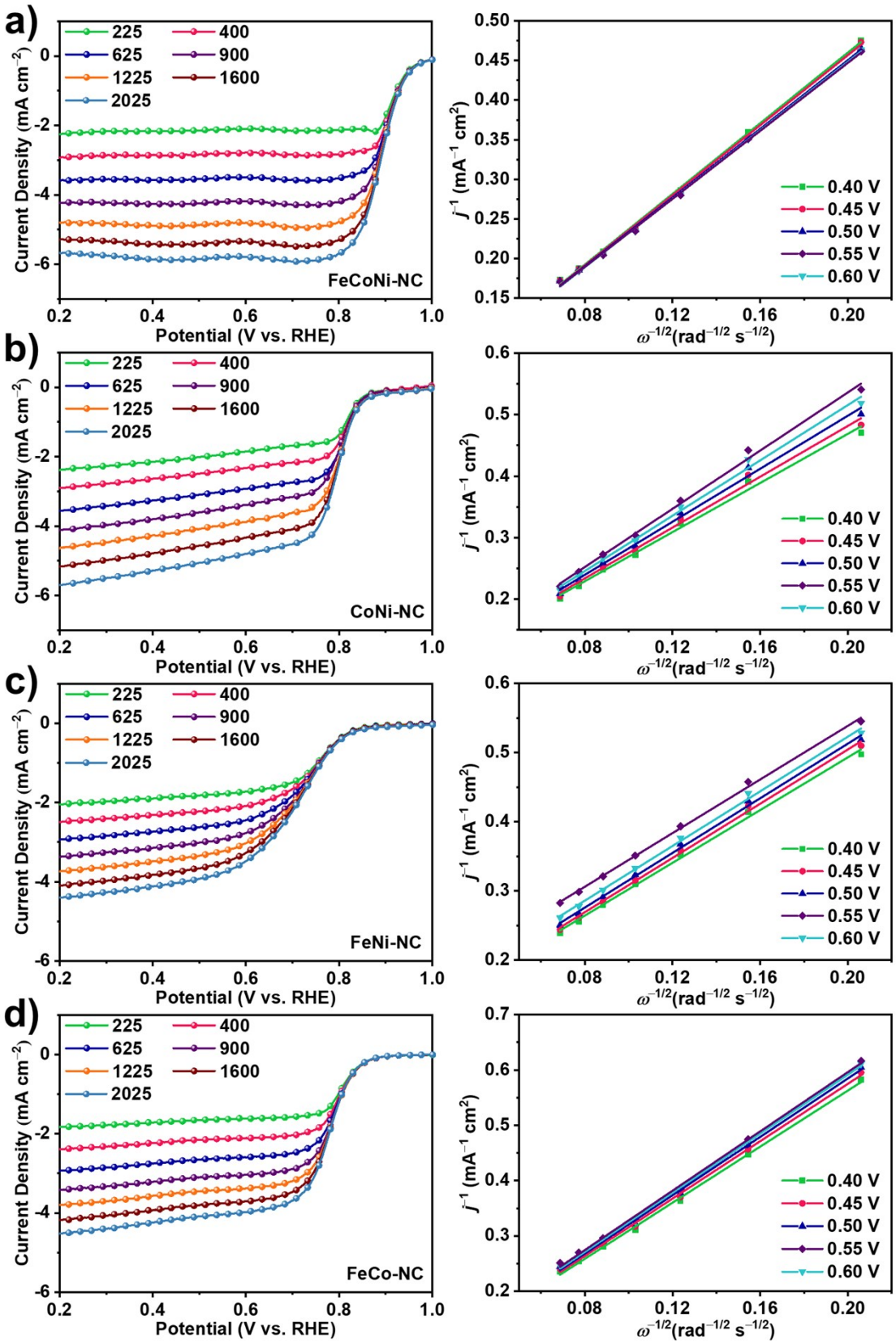

Figure S17. ORR linear sweep voltammetry (LSV) polarization curves and corresponding K-L plots for (a) FeCoNi-NC, (b) CoNi-NC, (c) FeNi-NC and (d) FeCo-NC.

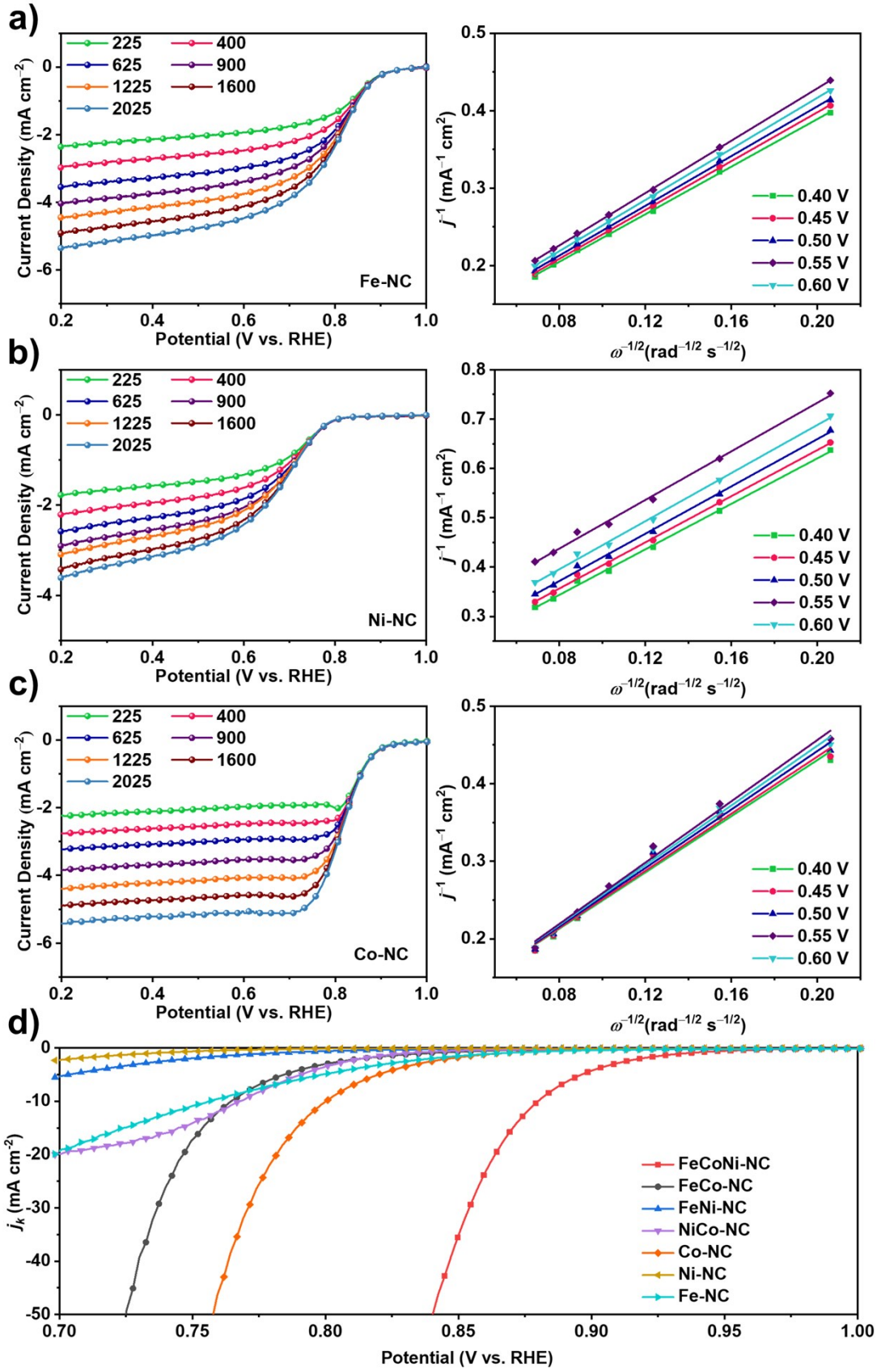

Figure S18. ORR LSV polarization curves and corresponding K-L plots for (a) Fe-NC, (b) Ni-NC and (c) Co-NC. (d) Kinetic current density of the samples over 0.70-1.00 V (vs. RHE).

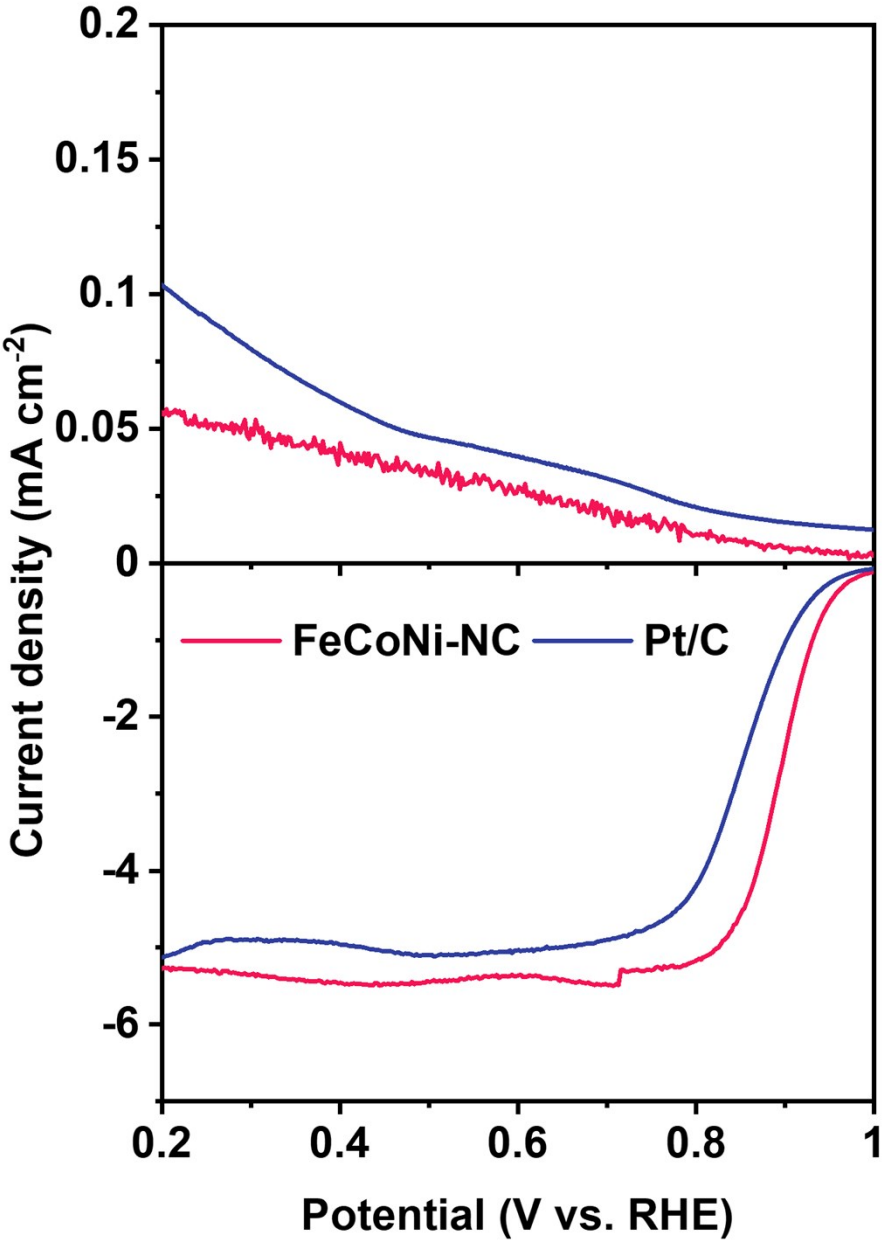

Figure S19. LSV polarization curves recorded from RRDE of FeCoNi-NC and reference Pt/C.

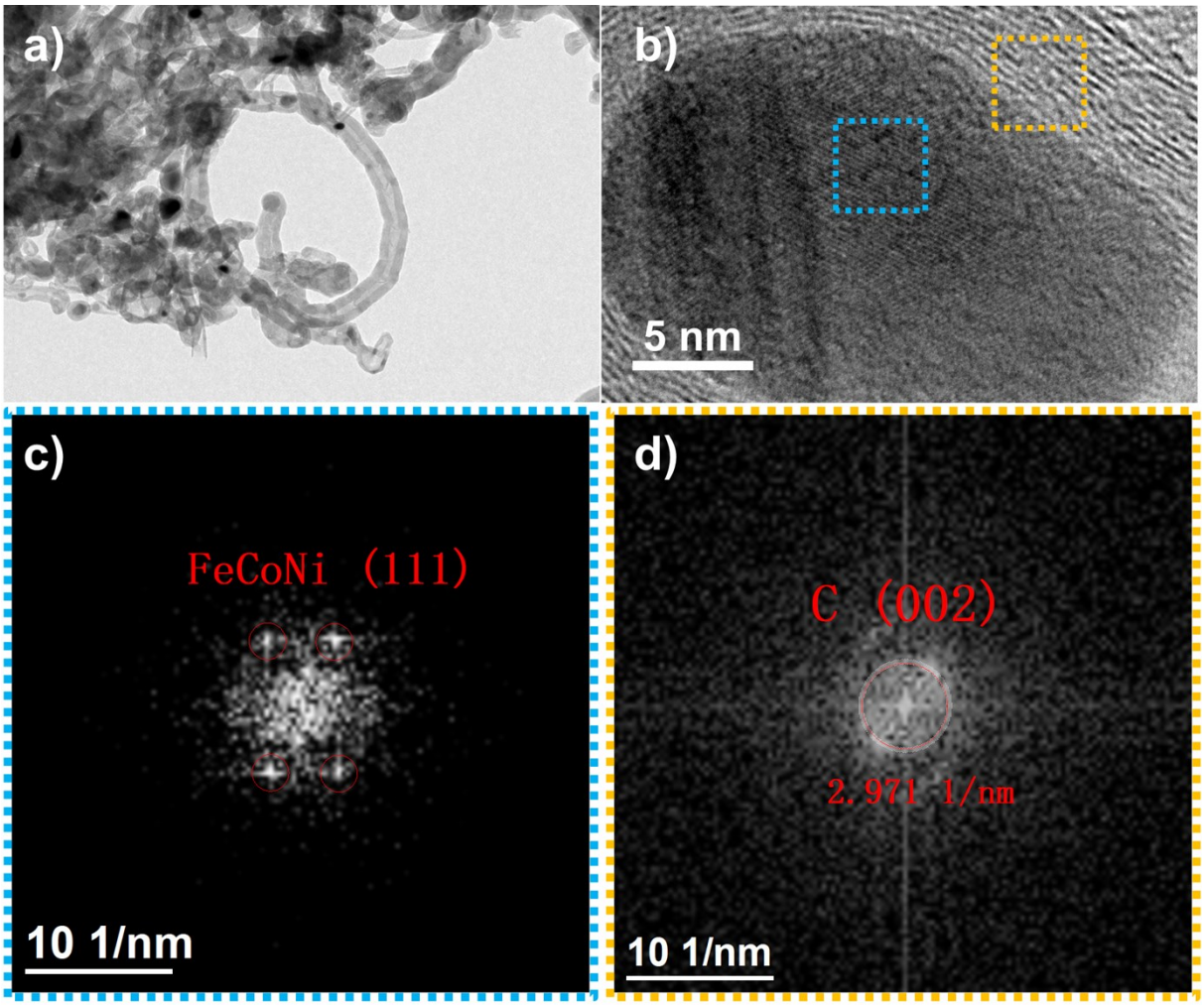

Figure S20. (a, b) TEM images for FeCoNi-NC after ORR accelerated stress tests and (c, d) FFT patterns of the region enclosed in blue and orange dots from **b**.

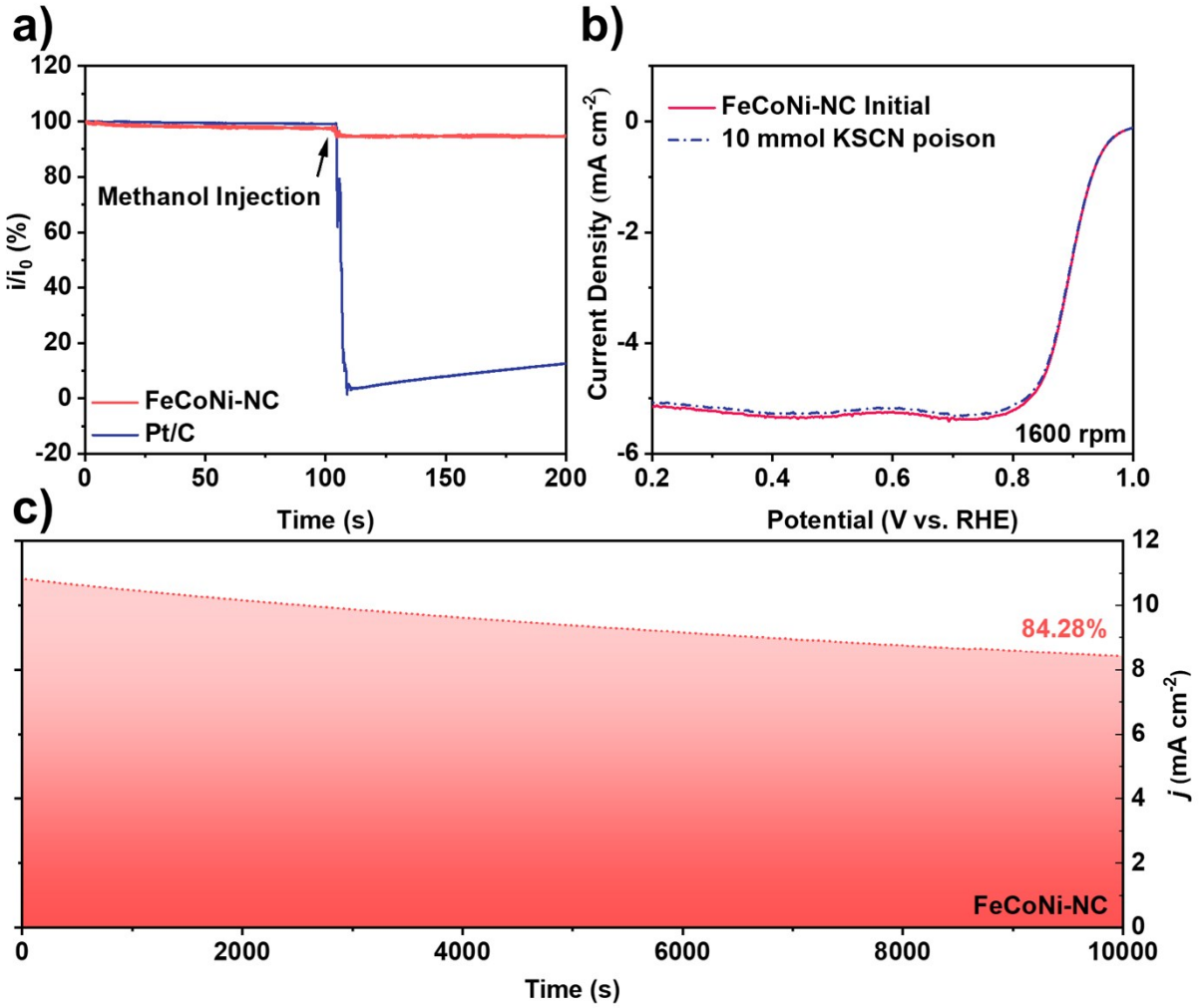

Figure S21. (a) Methanol tolerance tests for FeCoNi-NC and Pt/C. (b) KSCN poisoning test for FeCoNi-NC. (c) Chronoamperometric response of OER process for FeCoNi-NC.

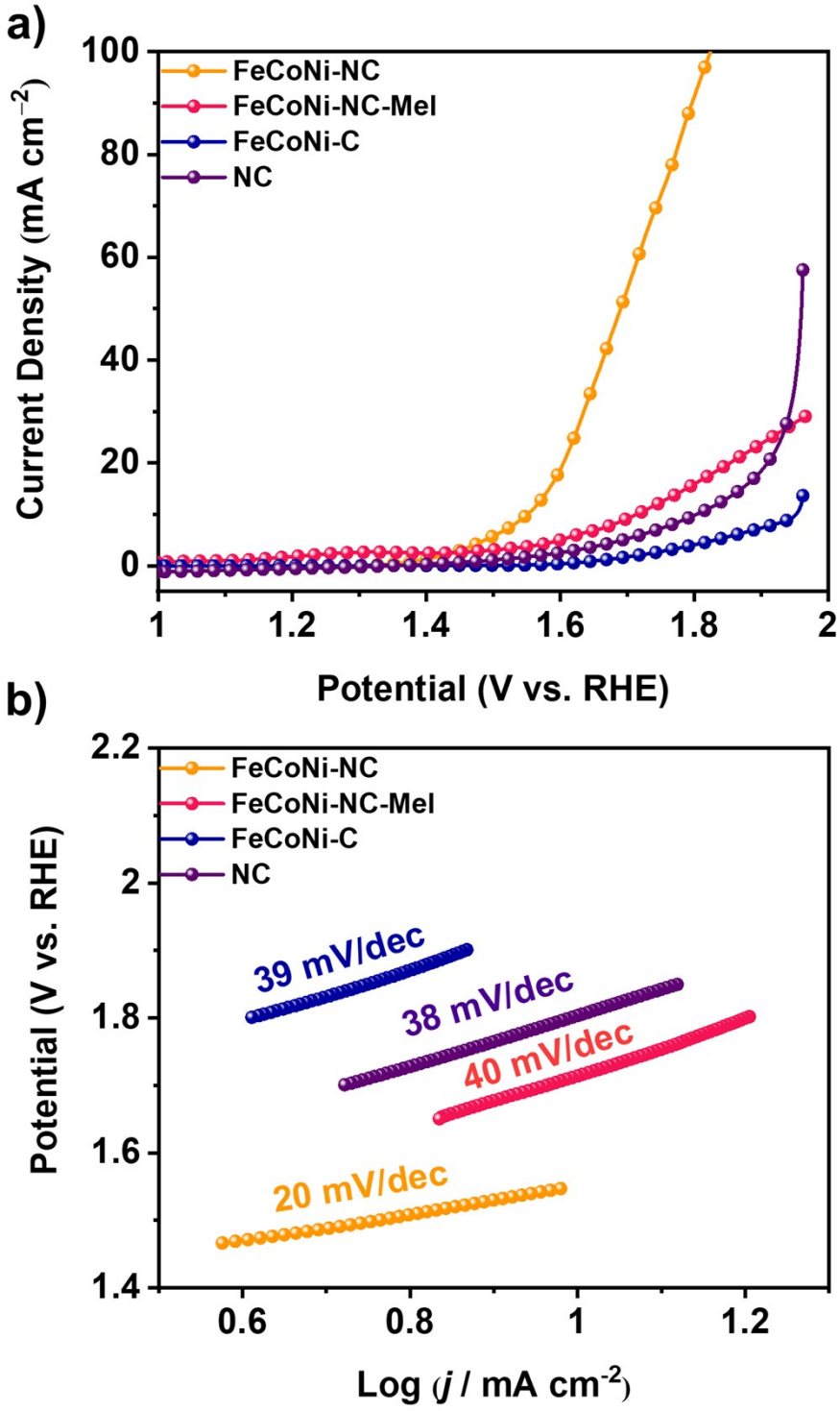

Figure S22. (a) OER LSV polarization curves and (b) OER Tafel plots for FeCoNi-NC, FeCoNi-NC-Mel, FeCoNi-C and NC.

Table S9. The ORR half-wave potential ($E_{1/2}$), OER onset potential ($E_{j=10}$) and overall overpotential (ΔE) for prepared simples and Pt/C-RuO_2.

Sample	$E_{1/2}$ (V vs. RHE)	$E_{j=10}$ (V vs. RHE)	ΔE (V vs. RHE)
FeCoNi-NC	0.89	1.54	0.65
FeCo-NC	0.76	1.76	1.00
FeNi-NC	0.72	1.75	1.03
CoNi-NC	0.80	1.68	0.88
Fe-NC	0.79	1.78	0.99
Co-NC	0.82	1.68	0.86
Ni-NC	0.69	1.95	1.26
Pt/C-RuO_2	0.85	1.71	0.86

Table S10. Comparison of the bifunctional activities of various state-of-the-art electrocatalysts for ORR and OER.

Type	Sample	$E_{1/2}$ (V)	$E_{j=10}$ (V)	ΔE (V)	References
FeCoNi	FeCoNi-NC	0.89	1.54	0.65	This work
FeCoNi	C@NCF-900	0.93	1.66	0.73	15
FeCoNi	CoNiFe-S MNs	0.78	1.49	0.71	11
FeCoNi	FeCo/FeCoNi@NCNTs-HF	0.85	1.71	0.86	20
FeCoNi	Fe_2Ni_2N/Co@NCNT	0.76	1.63	0.87	12
MnFeNi	$Mn_{0.5}(Fe_{0.3}Ni_{0.7})_{0.5}O_x$	0.84	1.57	0.73	13
FeCo	Co_2Fe_1@NC	0.85	1.65	0.80	24
FeCo	CoFe/N-GCT	0.79	1.67	0.88	16
FeCo	N-GCNT/FeCo-3	0.92	1.73	0.81	14
FeCo	FeCo-N_x-CN	0.89	1.67	0.78	25
FeCo	CoFe/SN-C-25	0.84	1.5	0.66	26
FeCo	FeCo-NPC-1100	0.79	1.6	0.81	27
FeNi	NiFe/N-CNT	0.75	1.52	0.77	21
CoNi	CoNi@NCNT/NF	0.87	1.54	0.67	18
Fe	S, N-Fe/N/C-CNT	0.85	1.60	0.75	28
Fe	NGM-CN-Fe	0.76	1.62	0.86	29
Co	NGM-Co	0.79	1.74	0.95	30
Co	Co-POC	0.83	1.70	0.87	31
W	W_2N/WC	0.83	1.55	0.72	7
Non-metal	SHG	0.87	1.56	0.78	32
Non-metal	DN-CP@G	0.79	1.76	0.97	33
Non-metal	N/E-HPC-900	0.85	1.61	0.76	34

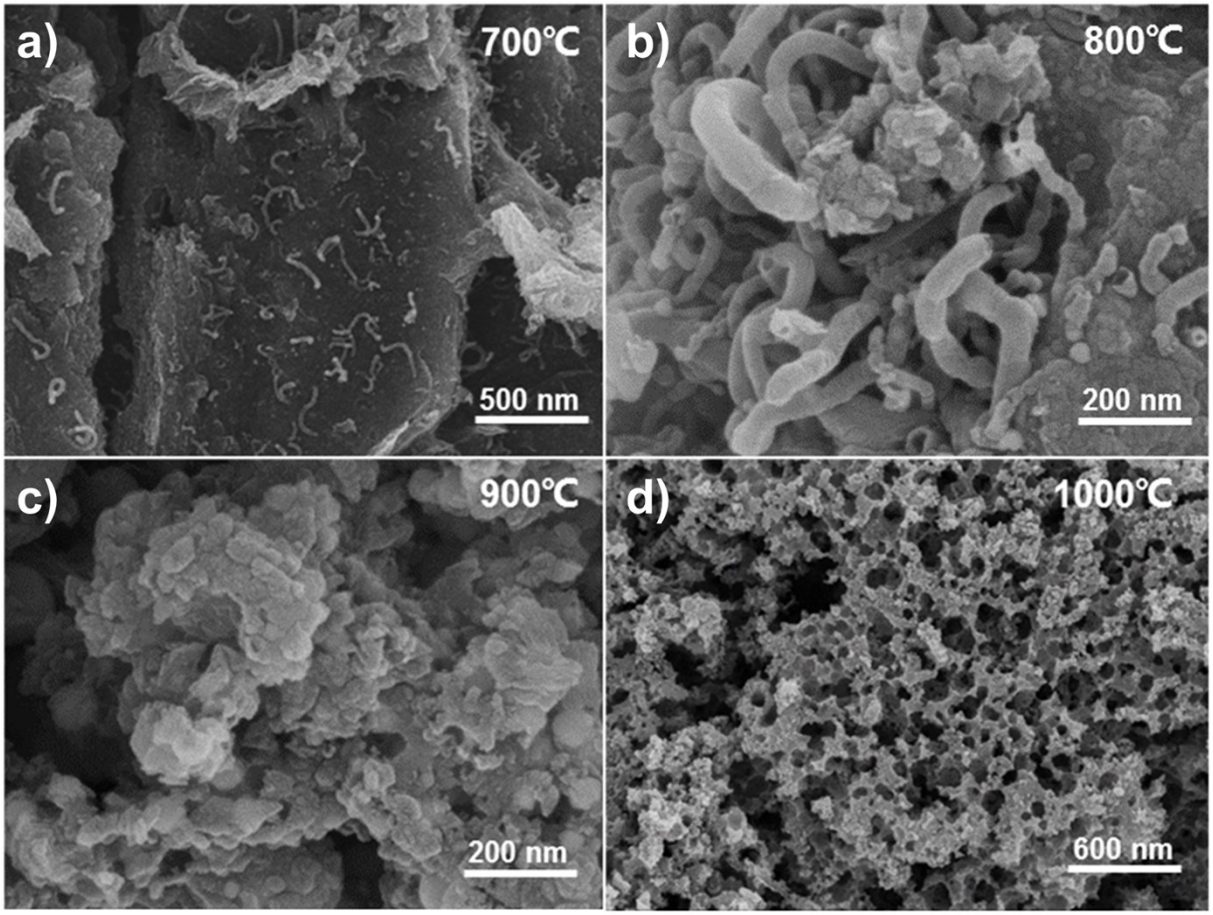

Figure S23. SEM images of FeCoNi-NC samples prepared at (a) 700 °C, (b) 800 °C, (c) 900 °C and (d) 1000 °C, respectively.

Table S11. Elemental contents of C, N, O, Fe, Co and Ni based on XPS analysis for trimetallic Fe-Co-Ni catalysts prepared in different temperatures.

Temperature	Chemical composition (at %)					
	C	N	O	Fe	Co	Ni
700 °C	77.44	12.06	9.15	0.56	0.34	0.47
800 °C	78.85	10.68	8.53	0.83	0.42	0.69
900 °C	93.73	2.41	0.03	0.35	0.15	0.31
1000 °C	90.66	2.51	6.27	0.25	0.14	0.15

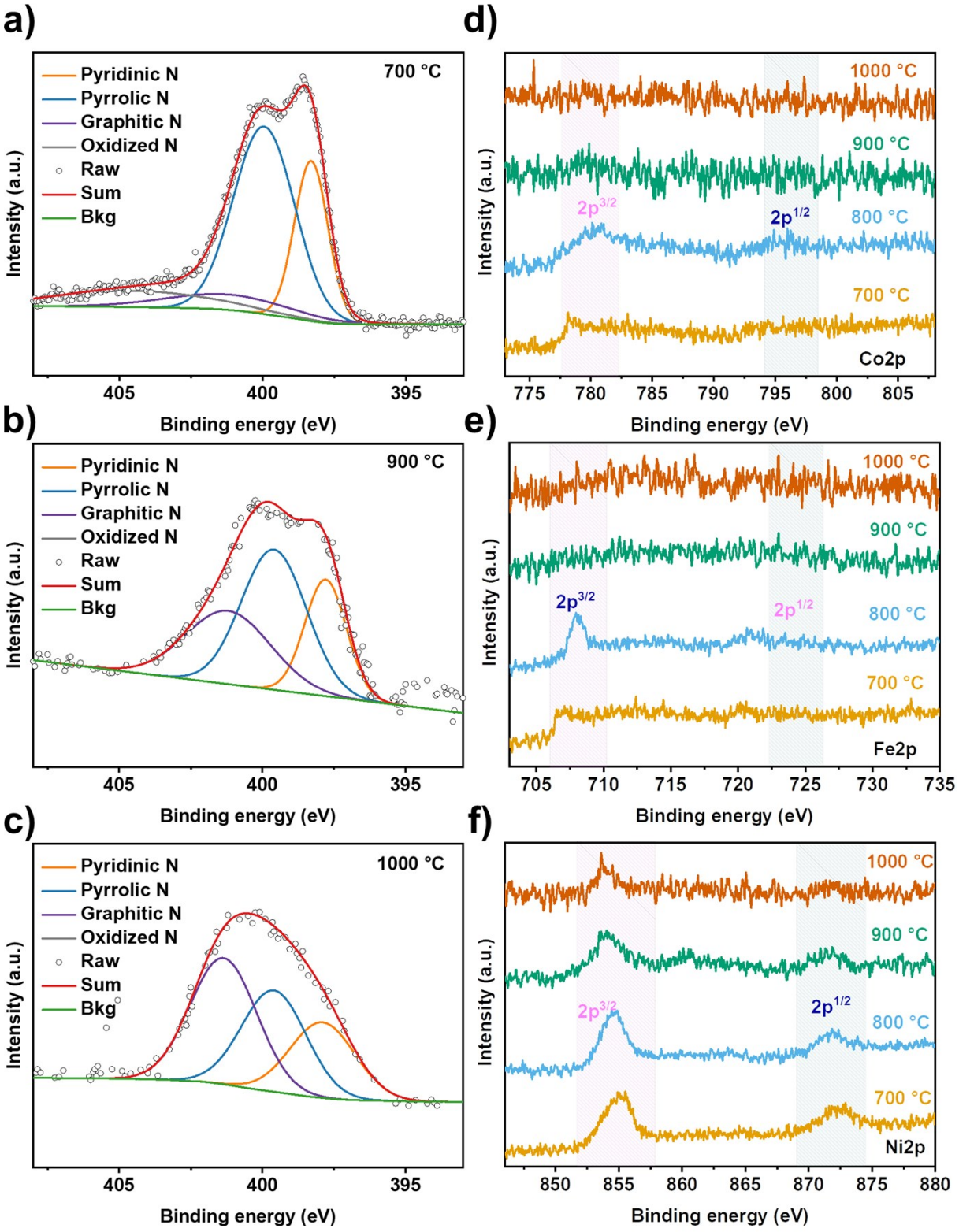

Figure S24. High-resolution (a-c) N 1s, (d) Co 2p, (e) Fe 2p and (f) Ni 2p XPS spectra of FeCoNi-NC samples prepared at different pyrolysis temperatures, respectively.

Table S12. Configuration of nitrogen based on N 1s high-resolution XPS analysis for trimetallic Fe-Co-Ni catalysts prepared in different temperatures.

Temperature	Configuration of nitrogen (%)			
	Pyridinic N	Pyrrolic N	Graphitic N	Oxidized N
700 °C	25.08	53.58	8.99	12.35
800 °C	48.47	38.65	11.92	0.95
900 °C	24.06	45.16	30.78	-
1000 °C	24.79	32.92	42.28	-

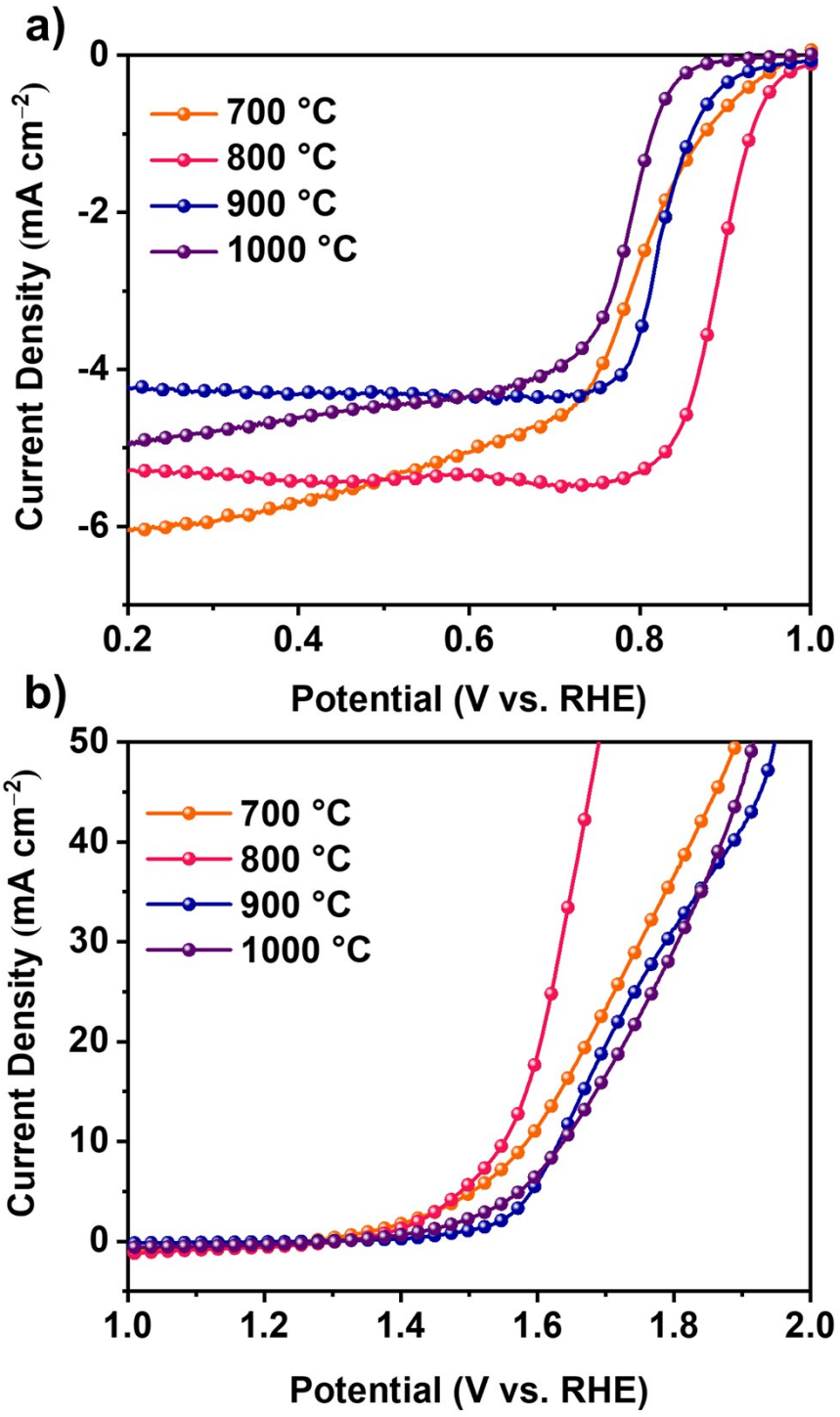

Figure S25. The electrocatalytic performance comparisons of FeCoNi-NC samples prepared at different pyrolysis temperature. (a) ORR LSV and (b) OER LSV polarization curves.

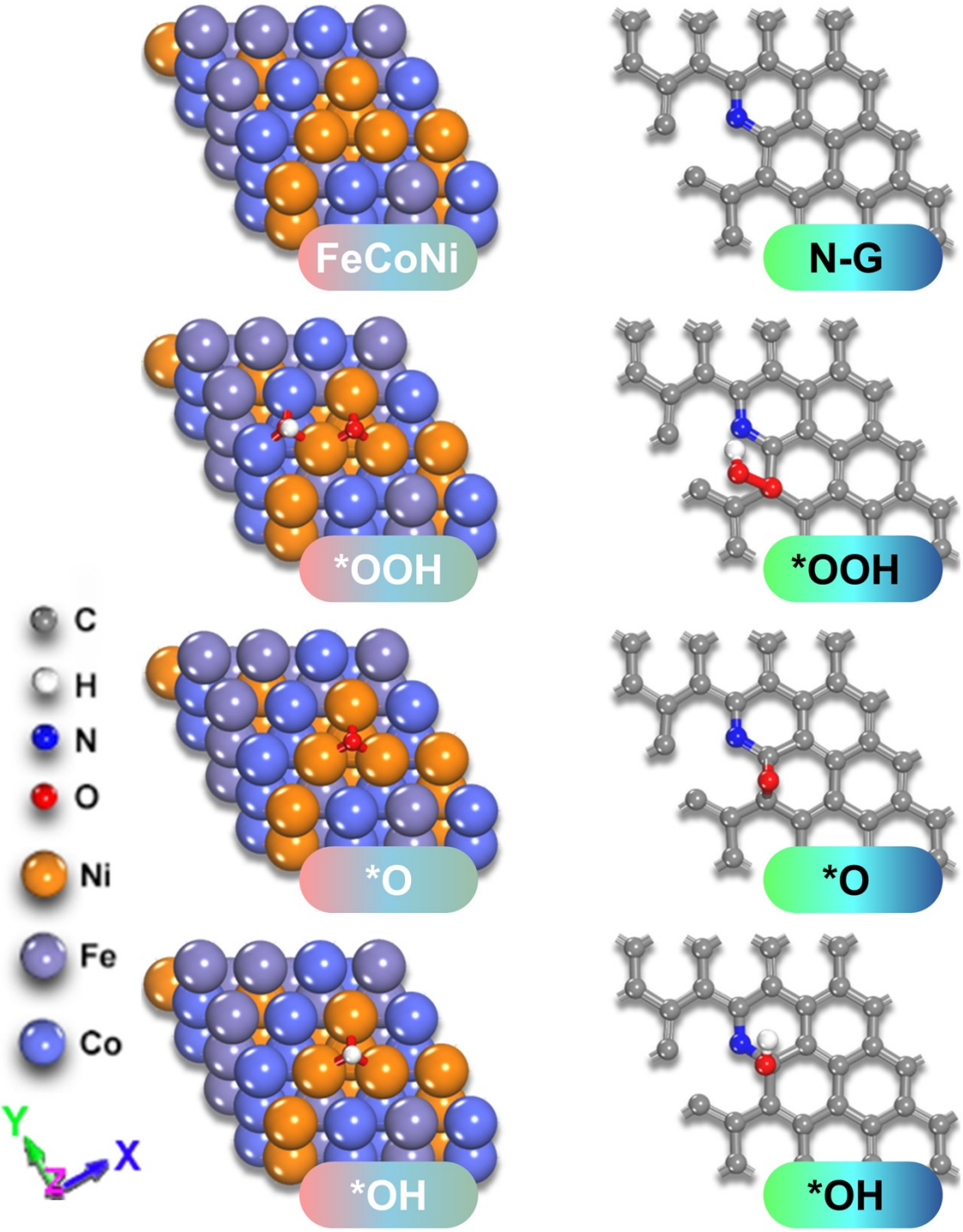

Figure S26. Theoretical models of pure Fe-Co-Ni alloy (FeCoNi), pyridinic-N doped graphene (N-G) and stable adsorption configurations of OER/ORR intermediates (*OOH, *O, *OH, where * in sign of the adsorption site). Due to the extreme strong interaction between OOH and FeCoNi, the optimized geometry of OOH on FeCoNi was split into two parts (O + OH) in the energy minimization *OOH configuration.

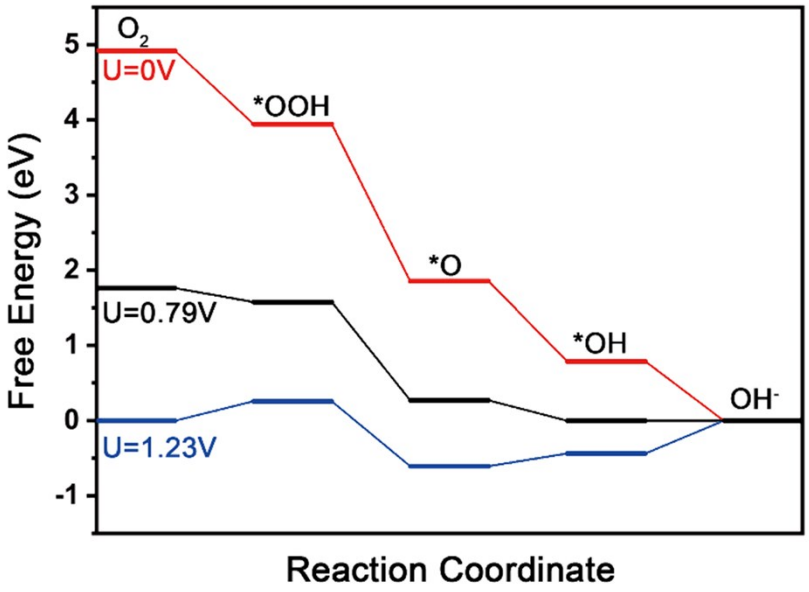

Figure S27. Free energy diagrams for FeCoNi-NC at zero potential, equilibrium potential and overpotential.

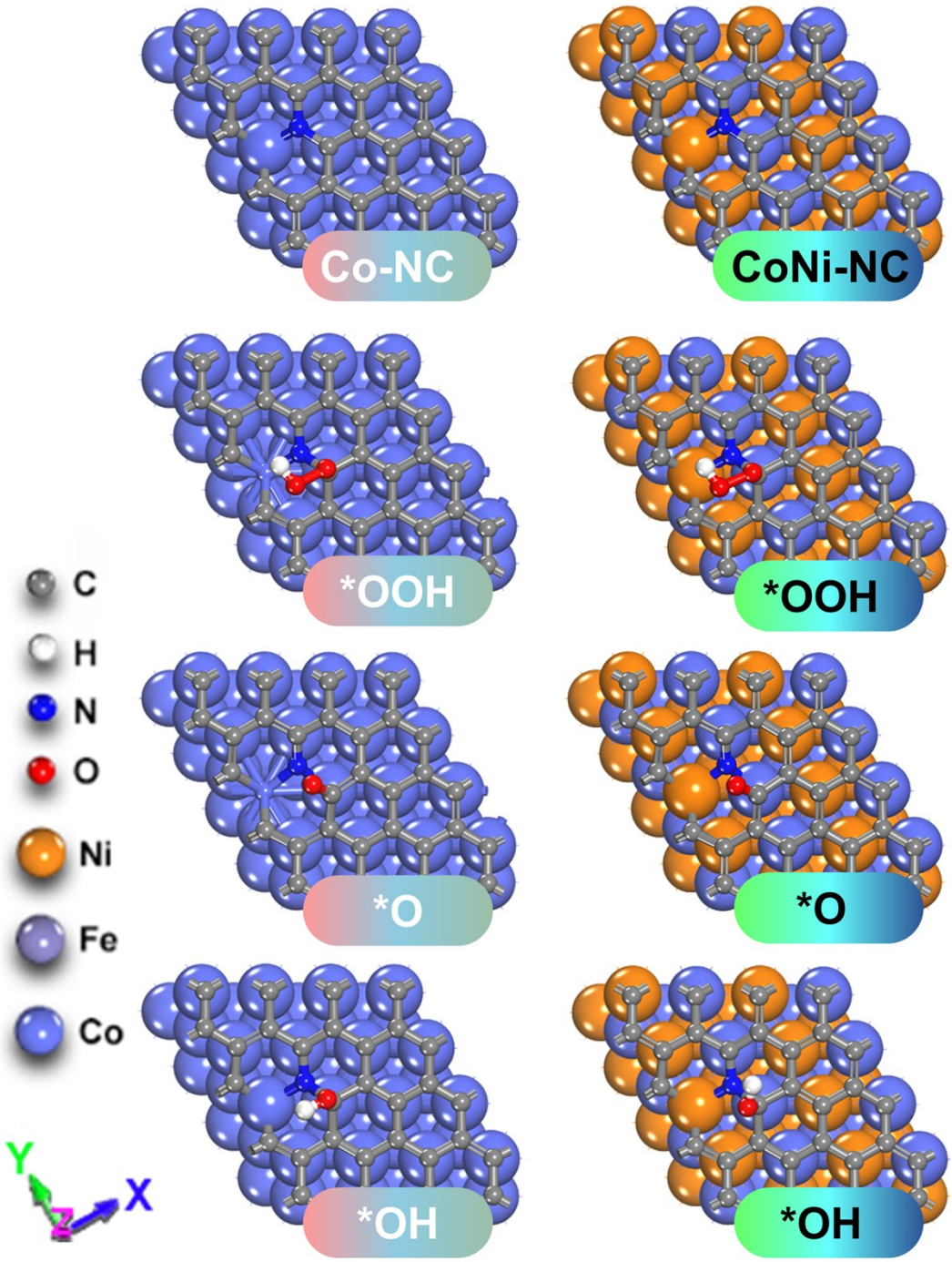

Figure S28. Theoretical models of pyridinic-N doped graphene coupled metallic Co (Co-NC), pyridinic-N doped graphene coupled bimetallic CoNi alloy (CoNi-NC) and stable adsorption configurations of OER/ORR intermediates (*OOH, *O, *OH, where * in sign of the adsorption site).

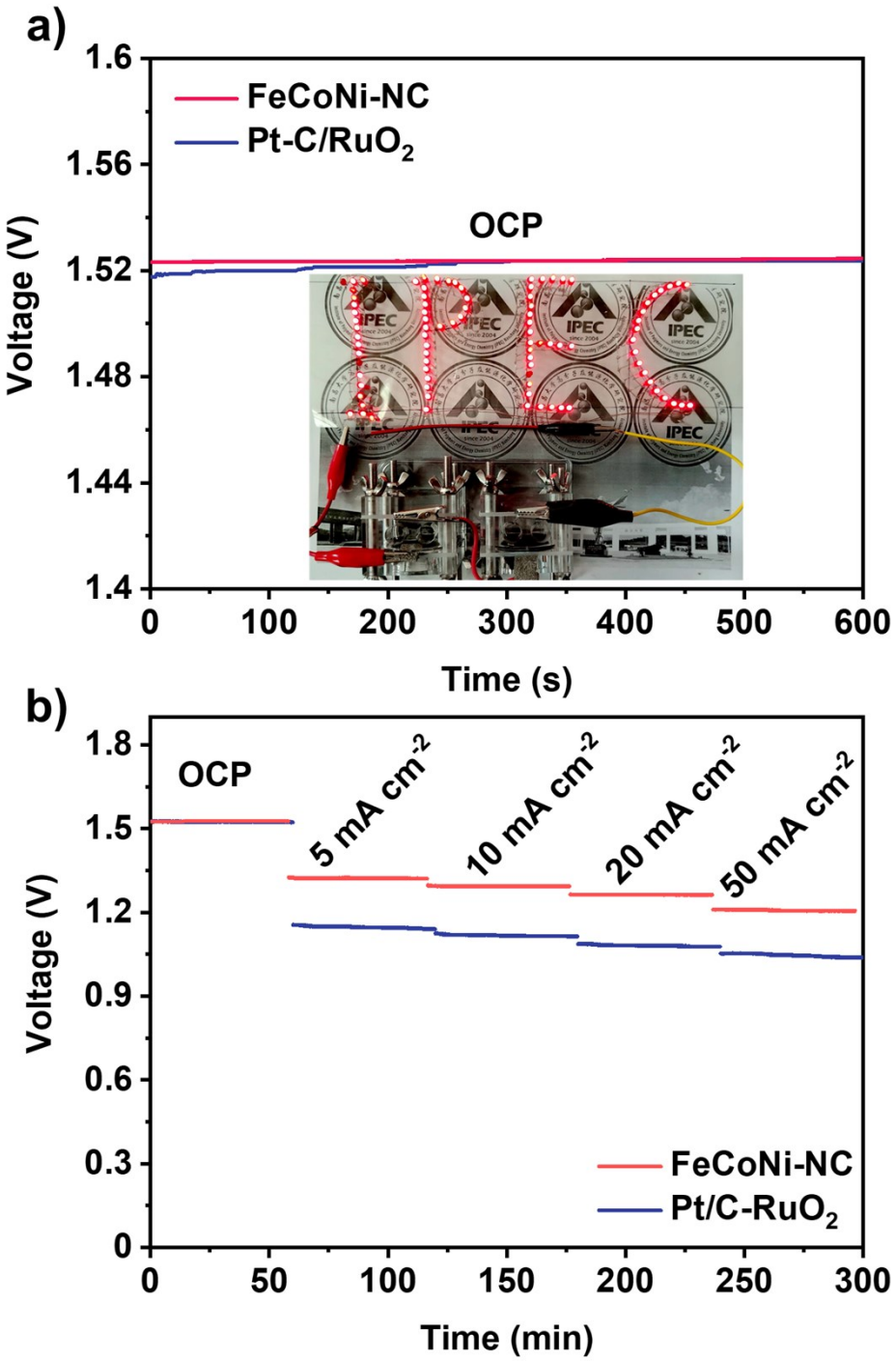

Figure S29. (a) The open-circuit potential curves (inset: photograph of a red LEDs array lighted by two FeCoNi-NC-based batteries in series). (b) Discharge curves of Zn-air batteries at different current densities.

Table S13. Comparison of the discharge performances for various state-of-the-art Zn-air batteries. All performances are reported in 6 M KOH.

Sample	Power Density/ mW cm^{-2}	Specific Capacity/ mAh g^{-1} (@ mA cm^{-2})	References
N-GCNT/FeCo-3	89	872@100	14
Ni-doped CoO NSs‖NiFe LDH	377	655@30	35
FeNC-S-Fe_xC/Fe	149	663@10	36
FeCo-DHO/NCNTs	326	793@20	19
$NiCo_2S_4$@g-C_3N_4-CNT	142	493@20	37
FeCo/Fe-CoNi@NCNTs-HF	156	762@10	20
Fe-N_x-C	96	641@10	38
Cu-SA/SNC	220	780@5	39
NCN-1000-5	207	672@10	40
Cu ISAS/NC	280	736@50	41
NiFe/N-CNT	301	698@50	21
Co_9S_8-NSHPCNF	280	823@20	42
FeCo(a)-ACM	160	776@20	43
Co_2Fe_1@NC	424	812@20	24
FeCoNi-NC	**315.2**	**804@100**	**This work**

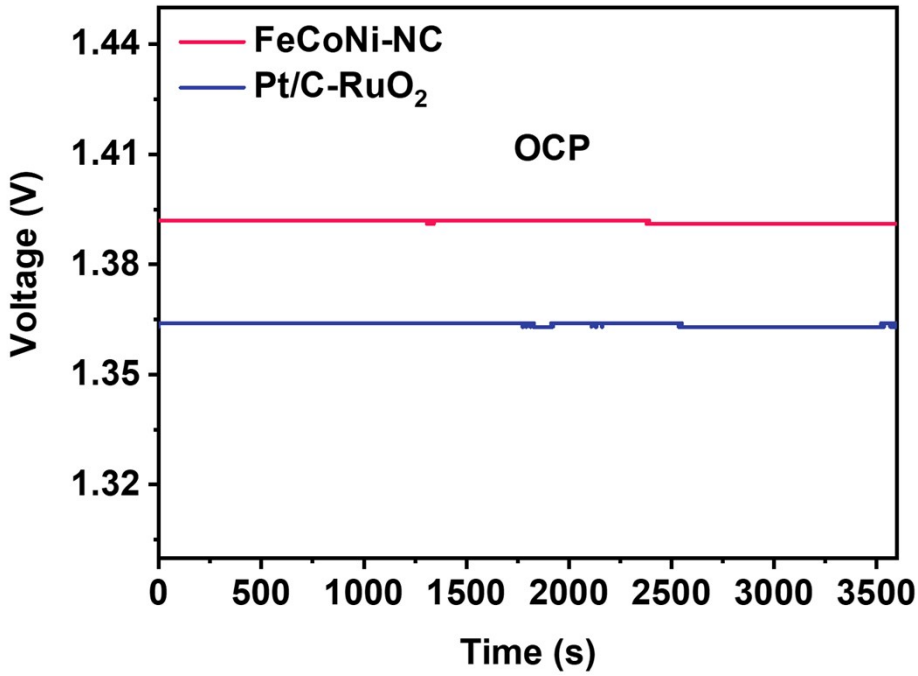

Figure S30. The open-circuit potential curves of all-solid-state Zn-air batteries using FeCoNi-NC and Pt/C-RuO2 as cathode catalyst.

REFERENCES

1 G. Kresse and J. Furthmüller, *Phys. Rev. B*, 1996, **54**, 11169–11186.

2 G. Kresse and D. Joubert, *Phys. Rev. B*, 1999, **59**, 1758–1775.

3 P. E. Blöchl, *Phys. Rev. B*, 1994, **50**, 17953–17979.

4 J. P. Perdew, J. A. Chevary, S. H. Vosko, K. A. Jackson, M. R. Pederson, D. J. Singh and C. Fiolhais, *Phys. Rev. B*, 1992, **46**, 6671–6687.

5 J. P. Perdew and Y. Wang, *Phys. Rev. B*, 1992, **46**, 12947–12954.

6 S. Grimme, J. Antony, S. Ehrlich and H. Krieg, *J. Chem. Phys.*, 2010, **132**, 154104.

7 J. Diao, Y. Qiu, S. Liu, W. Wang, K. Chen, H. Li, W. Yuan, Y. Qu and X. Guo, *Adv. Mater.*, 2020, **32**, 1905679.

8 A. J. Bard and L. R. Faulkner, *Electrochemical methods: Fundamentals and applications*, 1980.

9 X. Huang, T. Shen, T. Zhang, H. Qiu, X. Gu, Z. Ali and Y. Hou, *Adv. Energy Mater.*, 2020, **10**, 1900375.

10 L. Liu, Y. Wang, F. Yan, C. Zhu, B. Geng, Y. Chen and S. Chou, *Small Methods*, 2020, **4**, 1900571.

11 H. Yang, B. Wang, H. Li, B. Ni, K. Wang, Q. Zhang and X. Wang, *Adv. Energy Mater.*, 2018, **8**, 1801839.

12 M. Wu, G. Zhang, J. Qiao, N. Chen, W. Chen and S. Sun, *Nano Energy*, 2019, **61**, 86–95.

13 D. M. Morales, M. A. Kazakova, S. Dieckhöfer, A. G. Selyutin, G. V. Golubtsov, W. Schuhmann and J. Masa, *Adv. Funct. Mater.*, 2020, **30**, 1905992.

14 C.-Y. Su, H. Cheng, W. Li, Z.-Q. Liu, N. Li, Z. Hou, F.-Q. Bai, H.-X. Zhang and T.-Y. Ma, *Adv. Energy Mater.*, 2017, **7**, 1602420.

15 G. Nam, Y. Son, S. O. Park, W. C. Jeon, H. Jang, J. Park, S. Chae, Y. Yoo, J. Ryu, M. G. Kim, S. K. Kwak and J. Cho, *Adv. Mater.*, 2018, **30**, 1803372.

16 X. Liu, L. Wang, P. Yu, C. Tian, F. Sun, J. Ma, W. Li and H. Fu, *Angew. Chemie Int. Ed.*, 2018, **57**, 16166–16170.

17 S. Li, C. Cheng, X. Zhao, J. Schmidt and A. Thomas, *Angew. Chemie Int. Ed.*, 2018, **57**, 1856–1862.

18 W. Niu, S. Pakhira, K. Marcus, Z. Li, J. L. Mendoza-Cortes and Y. Yang, *Adv. Energy Mater.*, 2018, **8**, 1800480.

19 M. Wu, Q. Wei, G. Zhang, J. Qiao, M. Wu, J. Zhang, Q. Gong and S. Sun, *Adv. Energy Mater.*, 2018, **8**, 1801836.

20 Z. Wang, J. Ang, B. Zhang, Y. Zhang, X. Y. D. Ma, T. Yan, J. Liu, B. Che, Y. Huang and X. Lu, *Appl. Catal. B Environ.*, 2019, **254**, 26–36.

21 H. Lei, Z. Wang, F. Yang, X. Huang, J. Liu, Y. Liang, J. Xie, M. S. Javed, X. Lu, S. Tan and W. Mai, *Nano Energy*, 2020, **68**, 104293.

22 H. Khani, N. S. Grundish, D. O. Wipf and J. B. Goodenough, *Adv. Energy Mater.*, 2020, **10**, 1903215.

23 Q. Shi, Q. Liu, Y. Ma, Z. Fang, Z. Liang, G. Shao, B. Tang, W. Yang, L. Qin and X. Fang, *Adv. Energy Mater.*, 2020, **10**, 1903854.

24 T. Tang, W. Jiang, X. Liu, J. Deng, S. Niu, B. Wang, S. Jin, Q. Zhang, L. Gu, J. Hu and L. Wan, *J. Am. Chem. Soc.*, 2020, **142**, 7116–7127.

25 S. Li, C. Cheng, X. Zhao, J. Schmidt and A. Thomas, *Angew. Chemie Int. Ed.*, 2018, **57**, 1856–1862.

26 C. Li, E. Zhou, Z. Yu, H. Liu and M. Xiong, *Appl. Catal. B Environ.*, 2020, **269**, 118771.

27 B. Guo, Q. Ju, R. Ma, Z. Li, Q. Liu, F. Ai, M. Yang, S. Kaskel, J. Luo, T. Zhang and J. Wang, *J. Mater. Chem. A*, 2019, **7**, 19355–19363.

28 P. Chen, T. Zhou, L. Xing, K. Xu, Y. Tong, H. Xie, L. Zhang, W. Yan, W. Chu, C. Wu and Y. Xie, *Angew. Chemie Int. Ed.*, 2017, **56**, 610–614.

29 J. H. Zagal and M. T. M. Koper, *Angew. Chemie Int. Ed.*, 2016, **55**, 14510–14521.

30 C. Tang, B. Wang, H. Wang and Q. Zhang, *Adv. Mater.*, 2017, **29**, 1703185.

31 B. Li, C. Zhao, S. Chen, J. Liu, X. Chen, L. Song and Q. Zhang, *Adv. Mater.*, 2019, **31**, 1900592.

32 C. Hu and L. Dai, *Adv. Mater.*, 2017, **29**, 1604942.

33 C. Hang, J. Zhang, J. Zhu, W. Li, Z. Kou and Y. Huang, *Adv. Energy Mater.*, 2018, **8**, 1703539.

34 X. Peng, L. Zhang, Z. Chen, L. Zhong, D. Zhao, X. Chi, X. Zhao, L. Li, X. Lu, K. Leng, C. Liu,

W. Liu, W. Tang and K. P. Loh, *Adv. Mater.*, 2019, **31**, 1900341.

35 Y.-J. Li, L. Cui, P.-F. Da, K.-W. Qiu, W.-J. Qin, W.-B. Hu, X.-W. Du, K. Davey, T. Ling and S.-Z. Qiao, *Adv. Mater.*, 2018, **30**, 1804653.

36 Y. Qiao, P. Yuan, Y. Hu, J. Zhang, S. Mu, J. Zhou, H. Li, H. Xia, J. He and Q. Xu, *Adv. Mater.*, 2018, **30**, 1804504.

37 X. Han, W. Zhang, X. Ma, C. Zhong, N. Zhao, W. Hu and Y. Deng, *Adv. Mater.*, 2019, **31**, 1808281.

38 J. Han, X. Meng, L. Lu, J. Bian, Z. Li and C. Sun, *Adv. Funct. Mater.*, 2019, **29**, 1808872.

39 Z. Jiang, W. Sun, H. Shang, W. Chen, T. Sun, H. Li, J. Dong, J. Zhou, Z. Li, Y. Wang, R. Cao, R. Sarangi, Z. Yang, D. Wang, J. Zhang and Y. Li, *Energy Environ. Sci.*, 2019, **12**, 3508–3514.

40 H. Jiang, J. Gu, X. Zheng, M. Liu, X. Qiu, L. Wang, W. Li, Z. Chen, X. Ji and J. Li, *Energy Environ. Sci.*, 2019, **12**, 322–333.

41 Z. Yang, B. Chen, W. Chen, Y. Qu, F. Zhou, C. Zhao, Q. Xu, Q. Zhang, X. Duan and Y. Wu, *Nat. Commun.*, 2019, **10**, 3734.

42 W. Peng, Y. Wang, X. Yang, L. Mao, J. Jin, S. Yang, K. Fu and G. Li, *Appl. Catal. B Environ.*, 2020, **268**, 118437.

43 C. Chen, D. Cheng, S. Liu, Z. Wang, M. Hu and K. Zhou, *Energy Storage Mater.*, 2020, **24**, 402–411.